NAVAL POSTGRADUATE SCHOOL
Monterey, California

THESIS

REMOTE MEASUREMENT OF AEROSOL OPTICAL PROPERTIES USING THE NOAA POES AVHRR DURING ACE-1, TARFOX, AND ACE-2

by

Peter J. Smith

December 1998

Thesis Advisor: Philip A. Durkee

Approved for public release; distribution is unlimited.

REPORT DOCUMENTATION PAGE

Form Approved
OMB No. 0704-0188

1. AGENCY USE ONLY *(Leave blank)*	2. REPORT DATE	3. REPORT TYPE AND DATES COVERED
	December 1998	Master's Thesis

4. TITLE AND SUBTITLE
REMOTE MEASUREMENT OF AEROSOL OPTICAL PROPERTIES USING THE NOAA POES AVHRR DURING ACE-1, TARFOX AND ACE-2

5. FUNDING NUMBERS

6. AUTHOR(S)
Peter J. Smith

7. PERFOMING ORGANIZATION NAME(S) AND ADDRESS(ES)
Naval Postgraduate School
Monterey, CA 93943-5000

8. PERFORMING ORGANIZATION REPORT NUMBER

9. SPONSORING/MONITORING AGENCY NAME(S) AND ADDRESS(ES)

10. SPONSORING/MONITORING AGENCY REPORT NUMBER

11. SUPPLEMENTARY NOTES
The views expressed in this thesis are those of the author and do not reflect the official policy or position of the Department of Defense or the U.S. Government.

12a. DISTRIBUTION/AVAILABILITY STATEMENT
Approved for public release; distribution is unlimited.

12b. DISTRIBUTION CODE

13. ABSTRACT *(Maximum 200 words)*
A radiative transfer algorithm in the solar wavelengths for the NOAA POES AVHRR is presented for the cloud-free, marine atmosphere. This algorithm combines linearized, single-scattering theory with an estimate of bi-directional surface reflectance. Phase functions are parameterized using an aerosol distribution model and the ratio of radiance values measured in channels 1 and 2 of the AVHRR. Automated cloud screening and sun glint removal is included. Retrieved satellite aerosol optical depth (AOD) is compared to surface measured sunphotometer AOD collected during the International Global Atmospheric Chemistry (IGAC) Project's Second Aerosol Characterization Experiment (ACE-2) from June 16 to July 25, 1997. The comparison data set has a correlation coefficient of 0.88 with a standard error of 0.02 at both channel 1 and 2 wavelengths. Regional aerosol properties are examined with an emphasis on the differences between the ACE-1, TARFOX and ACE-2 regions. ACE-1 and ACE-2 regions have strong modes at AOD at around 0.1, but ACE-2 tails toward higher values consistent with urban and dust aerosol intrusion. The TARFOX region has a noticeable mode at AOD around 0.2, but has significant spread of AOD values consistent with the varied aerosol constituents in that area.

14. SUBJECT TERMS
Radiative transfer, NOAA AVHRR, aerosol optical depth, TARFOX, ACE-1, ACE-2

15. NUMBER OF PAGES
70

16. PRICE CODE

17. SECURITY CLASSIFICATION OF REPORT	18. SECURITY CLASSIFICATION OF THIS PAGE	18. SECURITY CLASSIFICATION OF ABSTRACT	20. LIMITATION OF ABSTRACT
Unclassified	Unclassified	Unclassified	UL

NSN 7540-01-280-5500

Standard Form 298 (Rev 2-89)
Prescribed by ANSI Std. 239-18
298-102

Approved for public release; distribution is unlimited

REMOTE MEASUREMENT OF AEROSOL OPTICAL PROPERTIES USING THE NOAA POES AVHRR DURING ACE-1, TARFOX AND ACE-2

Peter J. Smith
Lieutenant, United States Navy
B.S., United States Naval Academy, 1990

Submitted in partial fulfillment of the
requirements for the degree of

MASTER OF SCIENCE IN METEOROLOGY AND PHYSICAL OCEANOGRAPHY

from the

NAVAL POSTGRADUATE SCHOOL
DECEMBER 1998

Author: _____
Peter J. Smith

Approved by: _____
Philip A. Durkee, Thesis Advisor

_____
Carlyle H. Wash, Second Reader and
Chairman, Department of Meteorology

ABSTRACT

A radiative transfer algorithm in the solar wavelengths for the NOAA POES AVHRR is presented for the cloud-free, marine atmosphere. This algorithm combines linearized, single-scattering theory with an estimate of bi-directional surface reflectance. Phase functions are parameterized using an aerosol distribution model and the ratio of radiance values measured in channels 1 and 2 of the AVHRR. Automated cloud screening and sun glint removal is included. Retrieved satellite aerosol optical depth (AOD) is compared to surface measured sunphotometer AOD collected during the International Global Atmospheric Chemistry (IGAC) Project's Second Aerosol Characterization Experiment (ACE-2) from June 16 to July 25, 1997. The comparison data set has a correlation coefficient of 0.88 with a standard error of 0.02 at both channel 1 and 2 wavelengths. Regional aerosol properties are examined with an emphasis on the differences between the ACE-1, TARFOX and ACE-2 regions. ACE-1 and ACE-2 regions have strong modes at AOD at around 0.1, but ACE-2 tails toward higher values consistent with urban and dust aerosol intrusion. The TARFOX region has a noticeable mode at AOD around 0.2, but has significant spread of AOD values consistent with the varied aerosol constituents in that area.

TABLE OF CONTENTS

ACKNOWLEDGEMENTS

I would like to thank my advisor, Dr. Philip A. Durkee of the Department of Meteorology, Naval Postgraduate School, for his guidance and support during the development of this thesis. Additionally, I would like to thank Dr. Carlyle H. Wash for input as second reader.

Mr. Kurt Nielsen of the NPS Remote Sensing Laboratory was the backbone of this effort. Without his untiring computer assistance, especially with the UNIX operating system and FORTRAN this thesis would not have been completed.

I thank the following people for their direct and/or indirect support during this endevour: Dr. Haf Jonsson (CIRPAS), Dr. Q. Wang (NPS), LT Dan Eleuterio (NPS) and my wife, Lisa.

I would also like to thank the scientific teams at the NASA Ames, AERONET, and FISBAT for their contributions to the data used in this study.

I. INTRODUCTION

Atmospheric aerosols, whether naturally occurring or anthropogenic, impact the Earth's energy budget. Incoming solar radiation is scattered by these aerosols resulting in a net decrease in heating of the Earth's surface. Aerosols provide smaller condensation nuclei that increase cloud albedo at solar wavelengths, which again reduces heating at the Earth's surface. This is exactly the opposite affect of the currently highly publicized global warming trend due to greenhouse gases. According to Charlson et al. (1992) and the Intergovernmental Panel on Climate Change (IPCC) (1996), the cooling influence caused by aerosols maybe offsetting the greenhouse warming to a substantial degree. Schwartz and Andreae (1996) point out that if the aerosol forcing is significant and has negated much of the greenhouse forcing, then the resultant increase in global temperatures has come from a small residual forcing indicating a greater planetary temperature sensitivity. A greater sensitivity may result in accelerated global warming in the future. The uncertainty of aerosol forcing on the climate needs to be reduced to near the levels of uncertainty in greenhouse forcing in order to compare their weights. One avenue towards reducing this uncertainty is through satellite-based measurements of aerosol properties both globally and regionally.

Characterization of aerosol optical properties is equally important for the U.S. Navy. Since aerosols scatter and therefore degrade the system signal, this data can be used as input for electro-optical/infrared propagation models and tactical decision aids. Knowledge of aerosol optical properties is also important in the planning and

design of new weapons and sensors that operate at optical/infrared frequencies.

Ideally, characterization of aerosol optical properties would be accomplished through in situ measurements of radiative properties and aerosol size distributions. Sunphotometers, spectrometers, and radiometers provide very accurate pictures of these parameters, but their use are limited spatially and temporally. Additionally the employment of these tools is expensive and time consuming. The use of satellite-based radiometers, as suggested above, is a viable resource that allows greater spatial and temporal coverage. To measure the radiative properties in question the National Oceanic and Atmospheric Administration (NOAA) Polar Orbiting Environmental Satellite (POES) with its Advanced Very High Resolution Radiometer (AVHRR) can provide up to two passes per day for local analysis and a global picture twice per day. The AVHRR channel 1 (visible) and channel 2 (near infrared) possess the appropriate spatial and spectral resolution to measure optical radiative properties. This two solar channel capability is unique to the AVHRR instrument. Work done by Durkee et al (1991), Ronault and Durkee (1992) and Brown (1997) explore the use of the AVHRR two solar channel capability as a way to characterize phase scattering effects of aerosols. Aerosol retrieval techniques based on their work are used in this study.

Several experiments over the last few years have focused on aerosol properties and have provided ample field data for use in closure studies. These experiments include the International Global Atmospheric Chemistry (IGAC) Project's First Aerosol Characterization Experiment (ACE-1) in November 1995, Second Aerosol Characterization Experiment (ACE-2) in June 1997, and Tropospheric Aerosol Radiative Forcing Observational Experiment (TARFOX) in July 1996.

These experiments are important because they provide information on several different aerosol distributions that can represent a majority of the aerosol distributions found globally. ACE-1 focuses on aerosols in the remote marine atmosphere; TARFOX focuses on aerosols carried over the Western Atlantic Ocean from the United States; ACE-2 focuses on anthropogenically-modified aerosols and dust aerosols carried over the Eastern Atlantic Ocean from Europe and Africa.

The objectives of this thesis is twofold:

1) Validate aerosol optical depth retrievals using ACE-2 field observations of optical depth,

2) Conduct a regional analysis based on composites of retrieved optical properties during ACE-1, ACE-2, and TARFOX.

Chapter II describes the basic radiative transfer theory used in the satellite optical depth retrievals. Chapter III outlines the three experiments, the data sets and basic instrumentation used. Chapter IV describes the aerosol optical depth retrieval procedures and compositing procedures. Chapter V presents the results and Chapter VI discusses final conclusions and recommendations.

II. RADIATIVE TRANSFER THEORY

The mechanisms by which electromagnetic radiation is generated and how this radiation interacts with the atmosphere is described by radiative transfer theory (see Liou, 1980, for a complete description of the theory). The remote measurement of atmospheric properties by satellites necessitates an understanding of these theories. Simply stated, the radiation that is sensed by a satellite radiometer is the sum of the sources: emitted radiation and radiation scattered toward the satellite; and the sinks: absorbed radiation and the radiation scattered away from the satellite. Quantifying these sources and sinks leads to a complex equation called the Radiative Transfer Equation (RTE). Through assumptions about atmospheric radiative properties, the RTE can be simplified to a more usable form. In the case of calculating the effects of atmospheric aerosols we use a single scatter approximation along with a no-emission assumption. In a cloud free, marine environment, the short wave radiation sensed by a satellite radiometer is due mostly to the scattering of solar radiation by the molecular constituents of the atmosphere (Rayleigh scattering) and larger suspended aerosols (Mie scattering). Short wave here is defined as the visible (0.4 to 0.7 μm) and near infrared (0.7 to 1.0 μm) spectrum. Corrections for water vapor absorption at these wavelengths are on the order of 2-3% and corrections for ozone absorption are less than 5%. Although the no-emission assumption precludes terrestrial radiation playing a role, the ocean may reflect solar radiation. This is considered to be small except in certain cases such as sun glint and where high concentrations of particulate and phytoplankton exist. Contributions from sea surface foam and sub-surface reflectance can be accounted for with empirical

measurements; specular reflectance (sun glint) can be estimated. The radiative transfer process described here is illustrated in figure 2.1. The basic theories used to obtain aerosol optical properties in a cloud free, marine environment are presented in this chapter.

A. OPTICAL CHARACTERISTICS AND RADIATIVE TRANSFER

The optical characteristics of the atmosphere can be inferred through the measurement of their effects on radiative processes. Electromagnetic radiation interacts with the atmosphere in three basic mechanisms: absorption, scattering, and emission. Incoming solar radiation is attenuated in proportion to the density and absorbing characteristics of the atmosphere. The combination of absorption and scattering is termed extinction, and is quantified in the extinction coefficient given by:

$$\sigma_{ext} = \int_0^\infty \pi r^2 Q_{ext}(m, r) n(r) dr \quad (2.1)$$

where r is particle radius, πr^2 is particle cross-sectional area, $Q_{ext}(m,r)$ is the extinction efficiency factor, m is the complex index of refraction, and $n(r)$ is the number of particles for a given radius. Changes in the size, composition, and distribution of constituents or suspended particles in the atmosphere lead to a change in extinction. Therefore, the measurement of extinction can inversely lead to the characteristics of the atmosphere's particulate distribution.

The scattering of radiation is the largest contributing factor to extinction in the visible and near infrared wavelengths. Rayleigh (molecular) scattering can be calculated since the atmospheric molecular constituents are

nearly uniform both spatially and temporally (Durkee *et al.*, 1991). After the effects of molecular scattering are removed from the retrieved radiances, quantification of scattering effects due to suspended aerosols are left. The effect of scattering due to aerosols is approximated using Mie theory for spherical particles. For the cloud-free marine environment, the extinction coefficient can be approximated by the scattering coefficient:

$$\sigma_{scat} = \int_0^\infty \pi \ r^2 Q_{scat}(m,\lambda,r) n(r) dr \quad (2.2)$$

where $Q_{scat}(m,\lambda,r)$ is the scattering efficiency factor, representing the ratio of total energy scattered in all directions to incident energy.

Optical depth quantifies the atmospheric extinction through vertical integration of the extinction coefficient through the atmosphere, as represented by:

$$\delta = \int_0^H \sigma_{ext} dz \approx \int_0^H \sigma_{scat} dz \quad (2.3)$$

Satellite radiometers measure the radiative properties of the entire atmospheric column therefore quantification of total column optical depth is the objective of the satellite retrieval technique used in this study.

The above equations show the relationship between optical depth and the aerosol particle distribution. The extinction coefficient, and therefore the scattering coefficient, is a function of aerosol particle size, concentration and wavelength. The scattering efficiency factor weights the particle number differently for a given wavelength, so the radiance received at a given wavelength

has information on the number distribution of particles. This is the basis for the phase function parameterization used in the optical depth retrieval described in Chapter IV. Optical depth is a function of the extinction coefficient, so it follows that changes in aerosol particle size or distribution will be reflected in optical depth and satellite detected radiance.

B. RADIATIVE TRANSFER SOLUTION

The general form of the radiative transfer equation for a given solar wavelength in a plane parallel atmosphere (after Liou (1980)) is given by:

$$\mu \frac{dL_t(0; \mu, \phi)}{d\delta} = L_t(\delta, \Omega) - \frac{\omega_o}{4\pi} \int_{4\pi} L_t(\delta, \Omega) p(\Omega, \Omega') d\Omega - \frac{\omega_o}{4\pi} \pi F_o p(\Omega - \Omega_o) e^{-\delta/\mu_o} \qquad (2.4)$$

where μ is the cosine of satellite zenith angle (θ), μo is the cosine of Sun zenith angle (θo), φ is the relative azimuth between the satellite and Sun, L_t is diffuse radiance ($W/m^2\ \mu m\ sr$), Ω is the solid angle defined by θ and φ, ω_o is the single scattering albedo, p is the scattering phase function, and F_o is the incoming solar radiance at the top of the atmosphere. The total radiative energy in a beam, the energy scattered into the beam due to multiple scattering, and the energy scattered into the beam due to single scattering are the three terms on the right hand side of equation 2.4, respectively.

Multiple scattering is considered to be small in atmospheres with small optical depths such as the cloudless, marine atmosphere. The single scattering approximation

(after Liou (1980)), given by equation 2.5, results when the multiple scattering term is removed.

$$L_t = \frac{\omega_o \mu_o F_o}{4(\mu + \mu_o)} p(\psi_s)\left[1 - e^{-\delta\left(1/\mu_o + 1/\mu\right)}\right] \quad (2.5)$$

The argument for the phase function (p) is the scattering angle (ψ_s).

Durkee *et al.* (1991) show that in the cloud free, marine environment δ_a is small enough to reduce Equation 2.5 to:

$$L_a = \frac{\omega_o F_o}{4\mu} p(\psi_s)\delta_a \quad (2.6)$$

where the subscript "a" denotes aerosol related quantities. This linear relationship is obtained after removing contributions due to ozone, Rayleigh and ocean surface effects. This relationship also accounts for some multiple scattering especially where optical depth values are low (below $\delta \sim 0.5$).

Aerosol optical depth (δ_a) can be obtained using equation 2.6 if the remaining terms can be measured or calculated. Radiance at the satellite radiometer (L_a) due to aerosol scattering at a given wavelength is measured. The incoming solar radiance (F_o) is estimated given the sun-Earth geometry. The satellite zenith angle (represented by μ) is determined by the satellite-Earth geometry. The scattering phase function (P) is parameterized (see Chapter IV). The single scatter albedo (ω_o) is the ratio of the scattering coefficient to the extinction coefficient. As discussed earlier, the extinction coefficient is the sum

effect of absorption and scattering. Marine aerosols are weak absorbers therefore the scattering and extinction coefficients are approximately equal for this environment. This results in a single scatter albedo value of approximately one. However, there are some instances, such as when encountering combustion (carbon) and dust aerosols, when the single scatter albedo may be significantly less than one. Aerosol radiance (L_a) and scattering phase function (P) are described in detail below.

1. Aerosol Radiance (L_a)

The radiance measured by a satellite radiometer results from a combination of sources including Rayleigh (molecular) scattering, surface and sub-surface reflectance, sun glint and aerosol scattering. To isolate the measured radiance due only to aerosol scattering the additional sources must be removed. The radiance sources can be accounted for in a linear expression (after Gordon and Clark, 1980):

$$L_a = L_t - L_r - \left(L_s + L_g\right)\tau \quad (2.7)$$

where L_r is radiance due to Rayleigh Scatter, L_s is surface reflected radiance, L_g is Sun glint radiance, and τ is transmittance of the atmosphere. For satellite radiometer window channels in solar wavelengths, τ can be approximated as one with less than 10% error.

A correction to L_t is needed to account for ozone absorption in the upper atmosphere. L_t is divided by the slant-path transmittance due to atmospheric ozone as in Equation 2.8:

$$L_t = \frac{L_t}{e^{-\delta_{O_3}\left(\frac{1}{\mu_o}+\frac{1}{\mu}\right)}} \qquad (2.8)$$

where δ_{O_3} is ozone optical depth. Radiance contribution associated with Rayleigh scatter (L_r) is calculated using a two-stream model by Turner (1973). Surface reflected radiance comes from several sources. Surface reflectivity over the ocean, however, is minimal since the ocean is assumed to behave like a blackbody. This assumption, presented in Ramsey (1968), is based on ocean surface reflectivity less than 5% for red-visible wavelengths. The major contribution to L_s is surface reflectance from foam (white caps) and sub-surface reflectance from suspended particles/plant life. Koepke (1984) describes foam reflectance as a function of wind speed, foam age and foam coverage. Ignatov *et al.* (1995), based on Koepke (1984), calculate foam reflectance (at 0.63 μm) increasing from zero to 0.2% as the wind approaches 10 m/s. Additionally, Ignatov *et al.* (1995) calculate sub-surface reflectance (at 0.63 μm) in the open ocean, or coastal areas off the continental shelf in the absence of terrigenious influence, on the order of 0.14. This study approximates the combined effect of foam and subsurface reflectance as 0.5% at 0.63 μm and zero at 0.86 μm. Directional reflectance due to the variation in refractive index between the atmosphere and ocean is treated in the phase function term described below.

Contamination by specular glint (L_g) of the surface of the ocean for low Sun angles can causes problems by artificially raising measured radiances. Measured radiances are not used if they are suspect based on the satellite-Earth-Sun geometry and wind speed. In glint free areas L_g is assumed to be zero.

2. Scattering Phase Function (P)

The scattering phase function determines in which direction the radiation is scattered. The scattering phase function is dependent on the radiation wavelength, but more importantly it is dependent on the size, composition, and distribution of atmospheric constituents. For Rayleigh scattering, the phase function is well understood. For particles whose circumference is near that of the incident radiation's wavelength, aerosols in this case, Mie theory is used to quantify the scattering phase function. Knowledge of the aerosol size distribution and composition is necessary to accurately quantify the phase function, but it is precisely the aerosol characteristics desired as a result of this retrieval method. To parameterize the phase function, several methods may be used. A common approach, described by Shettle and Fenn (1979), incorporates a phase function empirically fit using measured averaged size distributions and characteristics for a region. Another method, used by Durkee *et al.* (1991), takes advantage of the sensitivity of the phase function to radiative differences between two (or more) wavelengths to parameterize the phase function. This is the method used in this study and is described in more detail in Chapter IV.

There are three scattering paths that we are concerned with when using a single scatter model and they must be accounted for with the phase function. The probability of direct scatter off an aerosol particle back to the satellite sensor is determined by using the back-scatter angle (90-180°) as the argument for the phase function. The other two paths are considered diffuse scatter reflecting off the ocean surface (bi-directional reflectance). These include forward scatter (0-90°) off an aerosol particle toward the ocean and reflection back to the satellite sensor, and

reflection off the ocean surface and forward scatter off an aerosol particle toward the satellite sensor. The diffuse scatter can be estimated using Fresnal reflection coefficients. This leads to an equation for the effective phase function:

$$p_{eff} = p_{-} + p_{+}\left[r_{\mu_o} + r_{\mu}\right] \quad (2.9)$$

where P_{eff} is the effective phase function, P_{-} is the value of the phase function at the back scattering angle, P_{+} is the value of the phase function at the forward scattering angle, and r is the Fresnel reflection coefficients at both μ_o and μ. Fresnel reflection coefficients are given in Equation (2.10):

$$r_{\theta} = 0.5\left[\left(\frac{\sin(\theta_i - \theta_t)}{\sin(\theta_i + \theta_t)}\right)^2 + \left(\frac{\tan(\theta_i - \theta_t)}{\tan(\theta_i + \theta_t)}\right)^2\right] \quad (2.10)$$

where θ_i is the angle of incidence and θ_t is the angle of transmission. From Snell's law, $\theta_t = \sin^{-1}(\sin(\theta_I)/m))$ where m is the index of refraction of seawater (1.33).

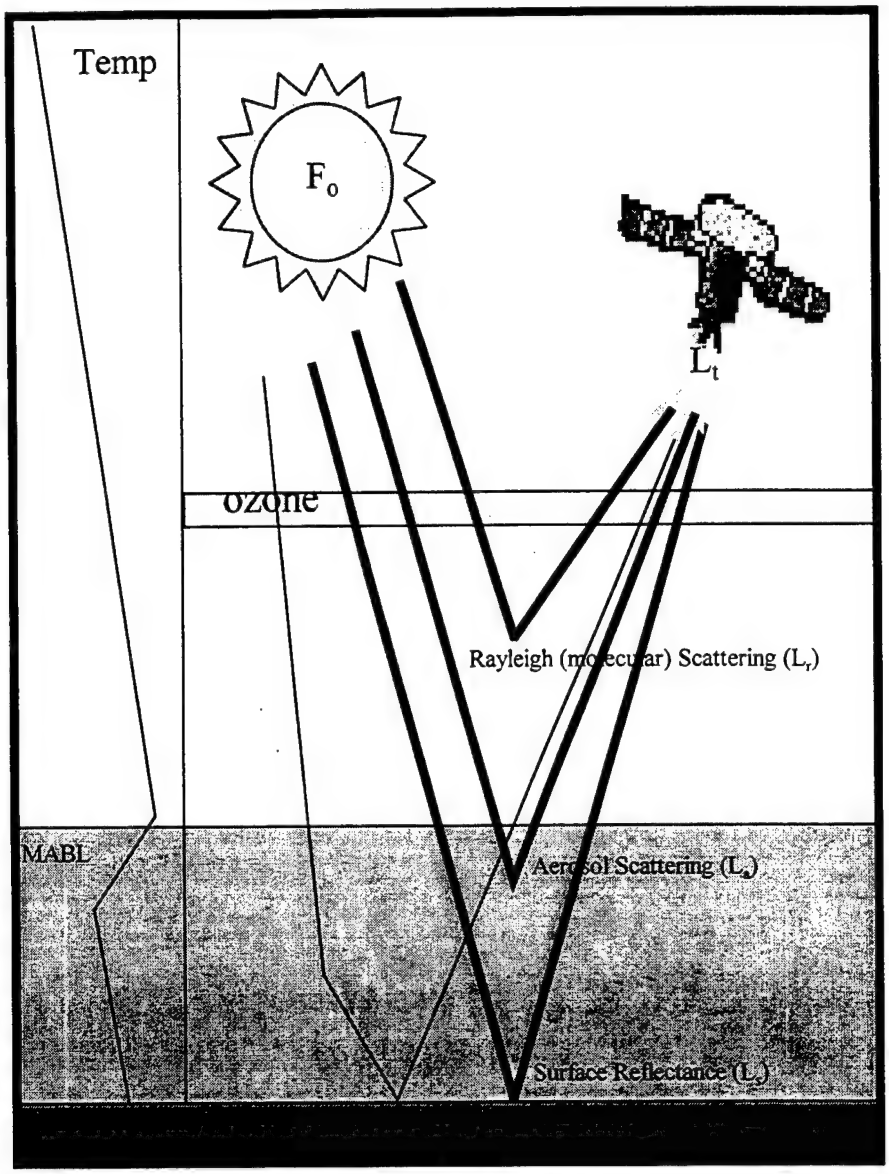

Figure 2.1. Radiative Transfer in the cloudless, marine environment. On the left, a typical atmospheric temperature profile depicting the marine atmospheric boundary layer (MABL) is included. Water vapor and aerosols are assumed to be confined to the MABL. Various scattering paths of incoming solar radiation (F_0) from Sun to satellite are shown in the right panel. Radiance variations along these paths measured by satellite radiometers (L_t) are primarily caused by upper atmosphere ozone absorption, Rayleigh (L_r) and aerosol (L_a) scattering, and ocean surface reflectance (L_s) (Brown 1997).

III. DATA

In order to validate the optical depth retrieval method described in this study, reference data from ACE-2 were chosen based on the availability of surface and airborne sunphotometer measurements of optical depth. To the greatest extent possible, sunphotometer measurements are matched to satellite observations both spatially and temporally. The aerosol optical depth composites were produced using the validated retrieval method with AVHRR data collected during each of the three experiments. This chapter will briefly describe the data sets and instrumentation used to collect the data used in this study.

A. OVERVIEW OF EXPERIMENTS

The main goal of ACE-1 was to determine and understand the properties and controlling factors of aerosols in the remote marine atmosphere that are relevant to radiative forcing and climate. This experiment took place in the minimally polluted marine atmosphere of the southern ocean south of Australia from November 15 to December 15, 1995. This area was selected due to the relatively simple marine aerosol background and its distance from the Northern Hemisphere sulfate aerosols. This aerosol background can provide a baseline to compare with anthropogenically perturbed aerosols transported from the continents. Data was collected at two land based sites (Cape Grim, Tasmania and Macquarie Island), two ships (Australian R/V Southern Surveyor and NOAA R/V Discoverer), and one airplane (NCAR C-130). Full resolution NOAA-14 AVHRR data was downloaded

real-time in Hobart. Bates et al. (1998) provides an overview of ACE-1.

TARFOX was designed as a closure study to better understand the radiative forcing effects of aerosols. TARFOX was conducted in the continentally influenced environment off the eastern coast of the United States near Wallops Island, Virginia from 10-31 July 1996. During TARFOX, a variety of aerosol conditions ranging from relatively clean to moderately polluted were observed and measured. In situ measurements were conducted by airborne platforms including the University of Washington's (UW) C-131A and the United Kingdom's (UK) Meteorological Research Flight C-130 (see Russell *et al.*, 1996). Satellite imagery collected included full resolution NOAA 14 AVHRR data. The TARFOX Operations Summary (Whiting *et al.*, 1996) contains details of the field collection effort. Brown (1997) provides a validation of the methods used in this study from TARFOX field observations.

ACE-2 carried on the goals of ACE-1, but focused on anthropogenic aerosols from the European continent and desert dust from the African continent as they move over the North Atlantic Ocean. This experiment was carried out between 16 June and 25 July, 1997 and involved coordinated data collection by six aircraft, one ship, and ground stations on Tenerife, Portugal and Madeira. An overview on the ACE-2 objectives can be found in the experiment's Science and Implementation Plan (IGAC, 1995). NOAA-14 AVHRR data was collected in real-time during the exercise. Aerosol optical depth measurements from four different sunphotometers were used to validate aerosol optical depth values from the satellite retrieval. The NASA Ames Airborne Tracking Sunphotometer (AATS-14) was flown aboard the Center

for Interdisciplinary Remotely Piloted Aircraft Studies (CIRPAS) Pelican aircraft. The NASA Ames Airborne Tracking Sunphotometer (AATS-6) was operated aboard the R/V Vodyanitskiy. The ground station at Tenerife used a CIMEL Electronique 318A sun/sky scanning spectral radiometer and the ground station at Sagres, Portugal used both the UVISIR-1 and IR-RAD sunphotometers.

B. INSTRUMENTS

1. NOAA Advanced Very High Resolution Radiometer (AVHRR)

The AVHRR instrument is a component of the NOAA Polar Orbiting Operational Environmental Satellite (POES) series satellites. These satellites are in Sun synchronous orbit (883 km) and provide two passes per day in the morning and evening, respectively. The NOAA-14 data were used exclusively for this study due to sun-earth-satellite geometry necessary for the aerosol optical depth retrieval. The AVHRR instrument measures radiant and solar-reflected energy from sampled areas of the Earth in five spectral bands with a sub-satellite resolution of 1.1 km. Table 3.1 lists the characteristics of the individual radiometer channels for the AVHHR (Kidwell, 1995). Channels 1 and 2 are used in the optical depth retrieval. Channels 1 through 5 are used in the cloud screening analysis.

All AVHRR channels are calibrated prior to launch. Channels 1 and 2 of the AVHRR have no onboard calibration systems. Post calibration methods for these channels have been developed by the NOAA/NESDIS Office of Research Applications based on the results of Rao and Chen (1995). Calibration formulae are incorporated into the satellite image processing discussed in Chapter IV.

Channel	Band Widths (μm)
1 (Visible)	0.58 - 0.68
2 (NIR)	0.725 - 1.10
3 (IR)	3.55 - 3.93
4 (IR)	10.3 - 11.3
5 (IR)	11.5- 12.5

Table 3.1. NOAA AVHRR Radiometric Channels

2. NASA Ames Airborne Tracking Sunphotometer (AATS)

By tracking the Sun, the NASA AMES Airborne Tracking Sunphotometer measures the relative intensity of the direct incoming solar radiation in multiple spectral channels. This information is converted to optical depth (Livingston and Russell, 1997; Schmid *et al.*, 1999). The AATS-14 is the 14-channel variant and was flown aboard the CIRPAS pelican aircraft. Channel filters are at wavelengths from 380 to 1558 nm. By flying an aircraft at low altitudes in cloud-free regions within the atmospheric boundary layer, total column optical depth can be well approximated. For this data set the Pelican flew mostly off the Island of Tenerife in cloud free areas. The AATS-6 is the 6-channel variant and it was operated aboard the research vessel R/V Vodyanitskiy. Channel filters are at wavelengths from 380 to 1020 nm. The R/V Vodyanitskiy sailed mostly south of Portugal, near the Str. of Gibraltar collecting data in an area influenced by anthopogenic aerosols. NASA Ames performed instrument calibration prior to operation. These instruments are designed to maintain calibration within 1%

during operation. Resolution of optical depth is on the order of 0.01. (Matsumoto *et al.*, 1987).

3. CIMEL Electonique 318A Spectral Radiometer

The AERONET program (see Holben, 1998) uses the CIMEL Electronique 318A sun/sky scanning spectral radiometer. This solar powered all weather instrument is robotically pointed and has approximately a 1.2 degree full angle field of view. The radiometer makes only two basic measurements, either direct sun or sky. The direct sun measurements are made in eight spectral bands between 340 and 1020 nm. The instrument was located at 28.0° N 16.6° W and an altitude of 10 m on Tenerife Island. The network of instruments is calibrated twice per year and obtains aerosol optical thickness accuracy to less than 0.01 for wavelengths greater than 440 nm.

4. UVISIR-1 Sunphotometer and IR-RAD Sun-radiometer

The UVISIR-1 and IR-RAD instruments were located in Sagres, Portugal at 8.9° N 36.9° W and an altitude of 50 m. These instruments were operated by the Institute of Physics and Chemistry of the Upper and Lower Atmosphere (FISBAT), Bologna, Italy. The UVISIR-1 instrument scans at 12 wavelengths between 360 and 1050 nm with a scanning interval of 2 min. The IR-RAD instrument scans at 13 wavelengths between 400 and 3700 nm with a scanning interval of 3 min. A check of the calibration constant reliability is in progress, therefore the aerosol optical thickness accuracy is estimated at 0.01 in line with the other sunphotometers used in this study.

IV. OPTICAL DEPTH RETREIVAL AND COMPOSITING PROCEDURES

This chapter describes the procedures used to calculate aerosol optical depths from the satellite imagery and the procedures used to create the composite images for the three exercise areas.

A. SATELLITE IMAGE RETRIEVAL/DISPLAY

The NOAA POES High Resolution Picture Transmission (HRPT) data collected during the exercise periods were archived to 4mm data cartridges. The Terascan Earth Remote Sensing System (by SeaSpace Corporation) was used to retrieve and display this data at full resolution. Terascan system includes software that converts sensor radiance counts into albedo/brightness temperature and calculates required angles from Sun-Earth-satellite geometry A full suite of post processing enhancements is also included. This greatly aided in the optical depth analysis.

B. OPTICAL DEPTH RETRIEVAL

The optical depth retrieval technique used in this study is an automated process based on work done by Brown (1997). Terascan and FORTRAN 77 code are used to manipulate the satellite data and calculate the required information. Terascan commands are used to retrieve raw satellite images from the pass disk of the Terascan receiver system.

The FORTRAN code included a check for sun glint, a cloud screening algorithm, and all the radiative transfer calculations including optical depth. The sun glint check determined a probability of sun glint in a given pixel based on the Cox and Munk (1954) model. This process takes into account sun-satellite geometry and wind speed. A conservative 14 m/s was used for the wind speed over the entire image and the pixel was removed if the probability of

sun glint was greater than 35%. The cloud screening algorithm, based on Saunders and Kriebel (1988), applies the following tests to determine cloud contamination in a given pixel:

-Gross cloud check: The pixel was removed if the Channel 4 temperature was less than the sea surface temperature (additionally, if the channel 4 temperature was greater than 303 K the pixel was considered to be land).

-Spatial coherence: The pixel was removed if the standard deviation of the channel 4 temperature was greater than 0.1 K or the standard deviation of the channel 3 temperature was greater than 0.45.

-Dynamic reflectance threshold test: The pixel was removed if the channel 2 reflectance was greater than 15% and if the channel 4 minus channel 5 temperature difference is greater than zero. The temperature difference test allows for a high reflectance due to dust aerosols (used only for ACE-2).

-VIS/NIR ratio test: The pixel was removed if the ratio of channel 1 to channel 2 bi-directional reflectance was less than 1.33.

-Thin cirrus test: The pixel was removed if the difference between the channel 4 and channel 5 temperatures was greater than pre-computed clear sky values.

The radiative transfer calculations are discussed below. After these calculations, the radiative transfer output from the FORTRAN code was imported back into Terascan format for post-processing and enhancement.

C. RADIATIVE TRANSFER CODE

The radiative transfer solution (Equation 2.6) is calculated using FORTRAN code and follows the theory in Chapter II. Optical depth is the primary output along with the solution to Equation 4.2. The input wavelength used is the central value of the satellite channel's spectral band.

The calculation of specific input variables for Equation 2.6 is described below.

1. Solar Radiance, Ozone and Rayleigh Optical Depths

Input values for solar irradiance are taken from the *NOAA Polar Orbiter Data Users Guide* (Kidwell, 1995). The values are determined by calculating a weighted average of solar irradiance over the spectral band of satellite radiometer. Solar radiance is calculated by dividing solar irradiance by pi (E_o/π). E_o is corrected for variation in the Earth-Sun distance prior to input into the model. Input values for ozone and Rayleigh optical depths are based on those reported Elterman (1970). Table 4.1 lists the values of solar irradiance, and both ozone and Rayleigh optical depths used in these calculations.

Satellite	Radiometer	Ozone δ	Rayleigh δ	Eo (W/m^2 μm)
NOAA 14	AVHRR Ch 1	0.027	0.057	1628
NOAA 14	AVHRR Ch 2	0.0021	0.019	1030

Table 4.1. Values of Ozone and Rayleigh Optical Depths, and Solar Irradiance.

2. Scattering Phase Function

Mie theory can be used to calculate phase function if the aerosol size distribution is known. The aerosol distribution is not normally available unless *in situ* aerosol measurements are taken. Parameterization of the scattering phase function is necessary to solve the radiative transfer problem. The method used in this study takes advantage of the differences in the measured radiance at different wavelengths to parameterize the scattering phase function.

Durkee *et al.* (1991) proposed using the measured aerosol radiance differences in the AVHRR channel 1 (visible) and 2 (NIR) to parameterize the phase function. The scattering efficiency (Q_{scat}) of an aerosol distribution is wavelength dependent, therefor, when the radius of the aerosol is nearly equal to the radiation wavelength, Q_{scat} is a maximum. The ratio of the channel radiances will be larger for smaller size particle distributions and smaller for larger size particle distributions. Durkee *et al.* (1991) called this ratio the particle size parameter, S_{12}. Since S_{12} varies in each pixel of the satellite image, the scattering phase functions can be parameterized for each pixel, allowing variations in aerosol distributions in the optical depth retrieval.

Seven model aerosol size distributions (M0-M6) (based on Brown, 1997) were created. The scattering phase functions and extinctions for these models were calculated using Mie theory. The models include one single-mode log-normal distribution and six bi-modal log-normal distributions which follow the equation:

$$\frac{dN_j(r)}{dr} = \frac{N_j}{(2\pi)^{1/2}\sigma_j 2.3r}\exp\left\{-\frac{1}{2\sigma^2}\left(\frac{\ln r - \ln r_m}{\ln(10)}\right)^2\right\} \quad (4.1)$$

where j = 1,2, N is the number density, r_m is the mean radius and σ is the standard deviation of log(r).

The mode radii and standard deviations used are designed to model the typical variations of aerosol distributions in the marine atmosphere. The first mode in the distribution models of the background aerosol while the second mode in the distribution models ocean-produced aerosol. Table 4.2 lists the mode radii and standard deviations. Figures 4.1, 4.2, and 4.3 illustrate the

resulting aerosol size distributions and the corresponding scattering phase functions at 0.63 μm and 0.86 μm.

Model	Mode Radii (μm)	Number Density (N)	Std Dev (σ)
M0	0.1/0.0	1000/0	1.7/0.0
M1	0.1/0.3	1000/3	1.7/2.1
M2	0.1/0.3	1000/5	1.7/2.2
M3	0.1/0.3	1000/8	1.7/2.35
M4	0.1/0.3	1000/10	1.7/2.51
M5	0.1/0.3	1000/13	1.7/2.6
M6	0.1/0.3	1000/15	1.7/2.7

Table 4.2. Mode Radii, Number Density and Standard Deviations for Model Aerosol Size Distributions

S_{12} values are calculated using the model phase functions and extinctions in the following equation (based on linear single scattering theory):

$$S_{12} = \frac{L_{ch1}}{L_{ch2}} \approx \frac{p_{ch1} F_{o_{ch1}} \sigma_{extch1}}{p_{ch2} F_{o_{ch2}} \sigma_{extch2}} \quad (4.2)$$

S_{12} is corrected for water vapor absorption in AVHRR channel 2 after Mahony (1991) using the split-channel (channels 4 and 5) water vapor retrieval proposed by Dalu (1986). The resulting S_{12} values for each aerosol model are shown in Figure 4.4.

S_{12} values are calculated for each pixel from AVHRR channel 1 and channel 2 data. Computed S_{12} values along with scattering angle are entered into a look up table (LUT) that represents Figure 4.4. The model aerosol distribution (Figure 4.1) best represented by the observed radiance measurements is selected. By using the scattering angle and

selected model size distribution, phase function values are then selected from LUTs based on Figures 4.2 and 4.3.

An additional check was added for extremely clean environments. In some cases during ACE-1 and ACE-2 the measured aerosol radiance was so low that it was almost indistinguishable above the background (or bias) level. This resulted in an artificially high S_{12} and an incorrect aerosol model assumption. In these cases, defined by brightness counts less than 2.5 above bias, the aerosol model was set to M6. The M6 model is more typical of this clean environment. Optical depths were than recalculated based on the new phase function selection.

D. COMPOSITE PROCESS

The composite process consisted of grouping pixel values into bins and performing statistical calculations. 10 by 10 km bins were defined across a predetermined area of coverage. These areas were slightly larger than the exercise areas themselves. The values calculated by the radiative transfer code for each NOAA 14 pass during the exercise were summed and averaged over a bin. In some instances a standard deviation was calculated. Since the AVHRR resolution is approximately 1 km, there could be as many as 100 pixels per bin. Some manual and automated quality control was used. Each pass was manually screened for obvious errors such as optical depth values within the boundaries of a cloud field. One hundred pixels from each side of the image are removed to avoid sampling data from the edges of the pass where distortion exists. Summing all of the passes then created the area composite.

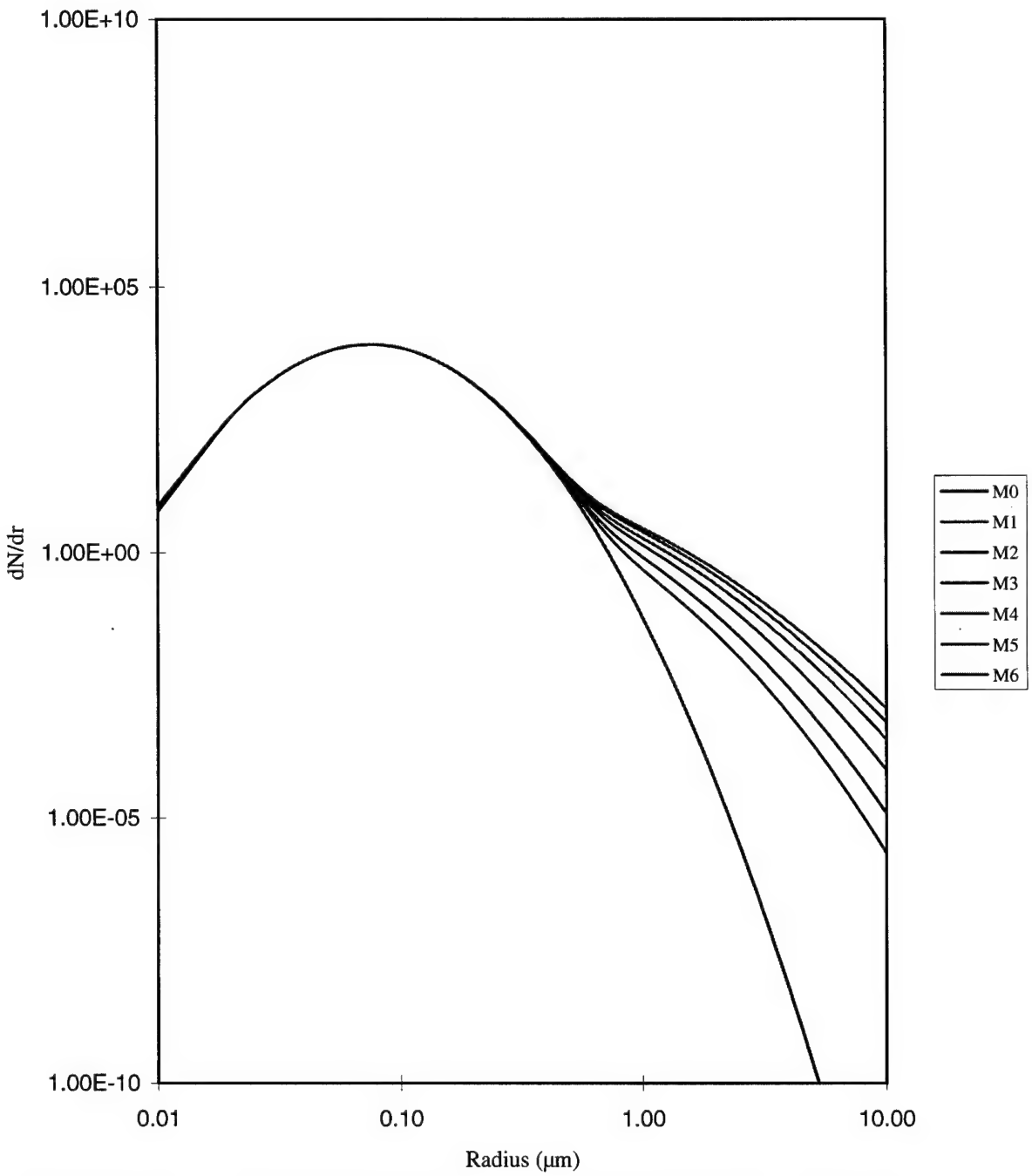

Figure 4.1. Model Aerosol Size Distributions. M0-M6 correspond to model two-mode, lognormal aerosol distributions with M0 representing the background (continental) aerosol mode and M6 representing the largest oceanic aerosol mode (From Brown 1997).

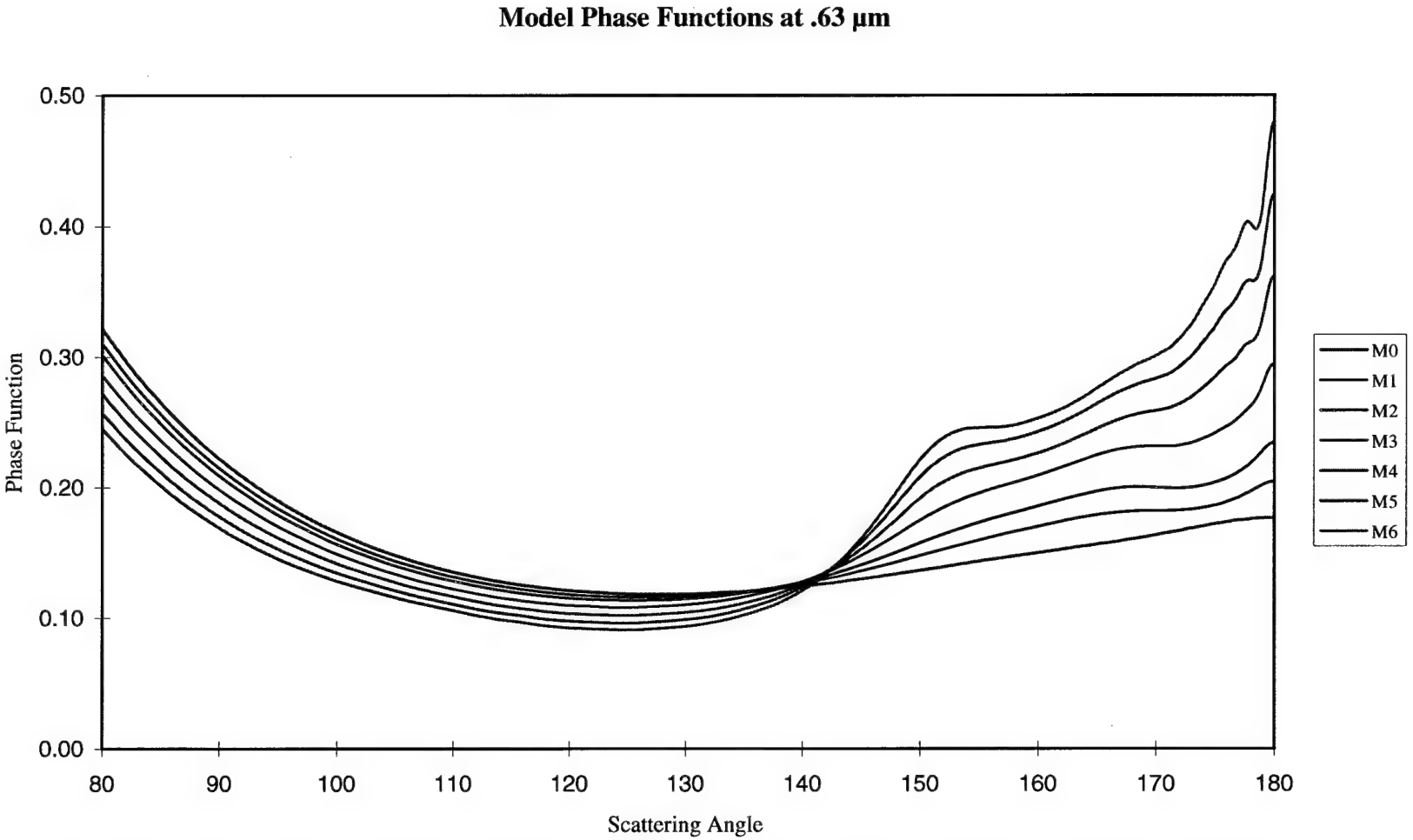

Figure 4.2. Model Phase Functions at 0.63 µm. M0-M6 correspond to model two-mode, lognormal aerosol distributions with M0 representing the background (continental) aerosol mode and M6 representing the largest oceanic aerosol mode (From Brown 1997).

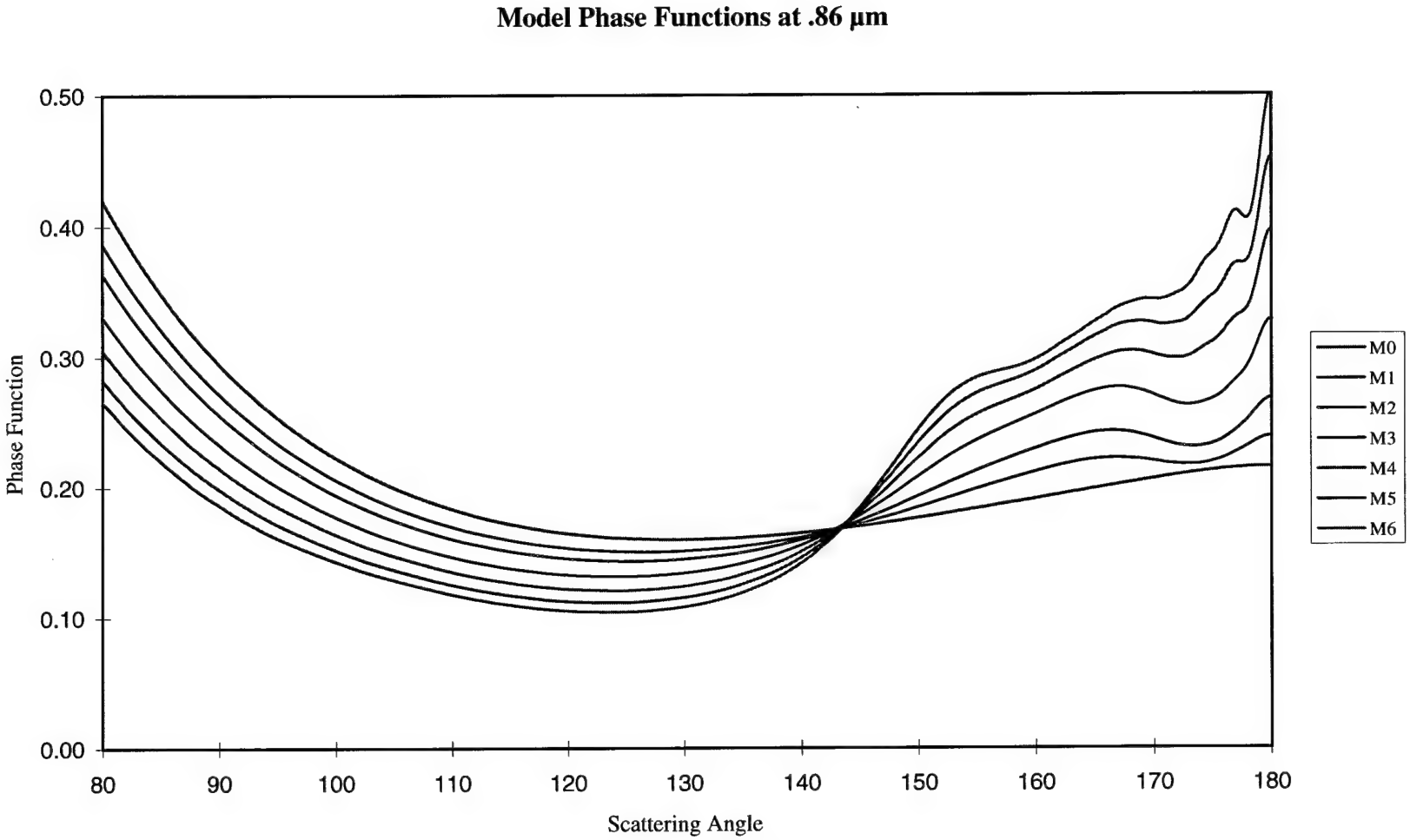

Figure 4.3. Model Phase Functions at 0.86 µm. M0-M6 correspond to model two-mode, lognormal aerosol distributions with M0 representing the background (continental) aerosol mode and M6 representing the largest oceanic aerosol mode (From Brown 1997).

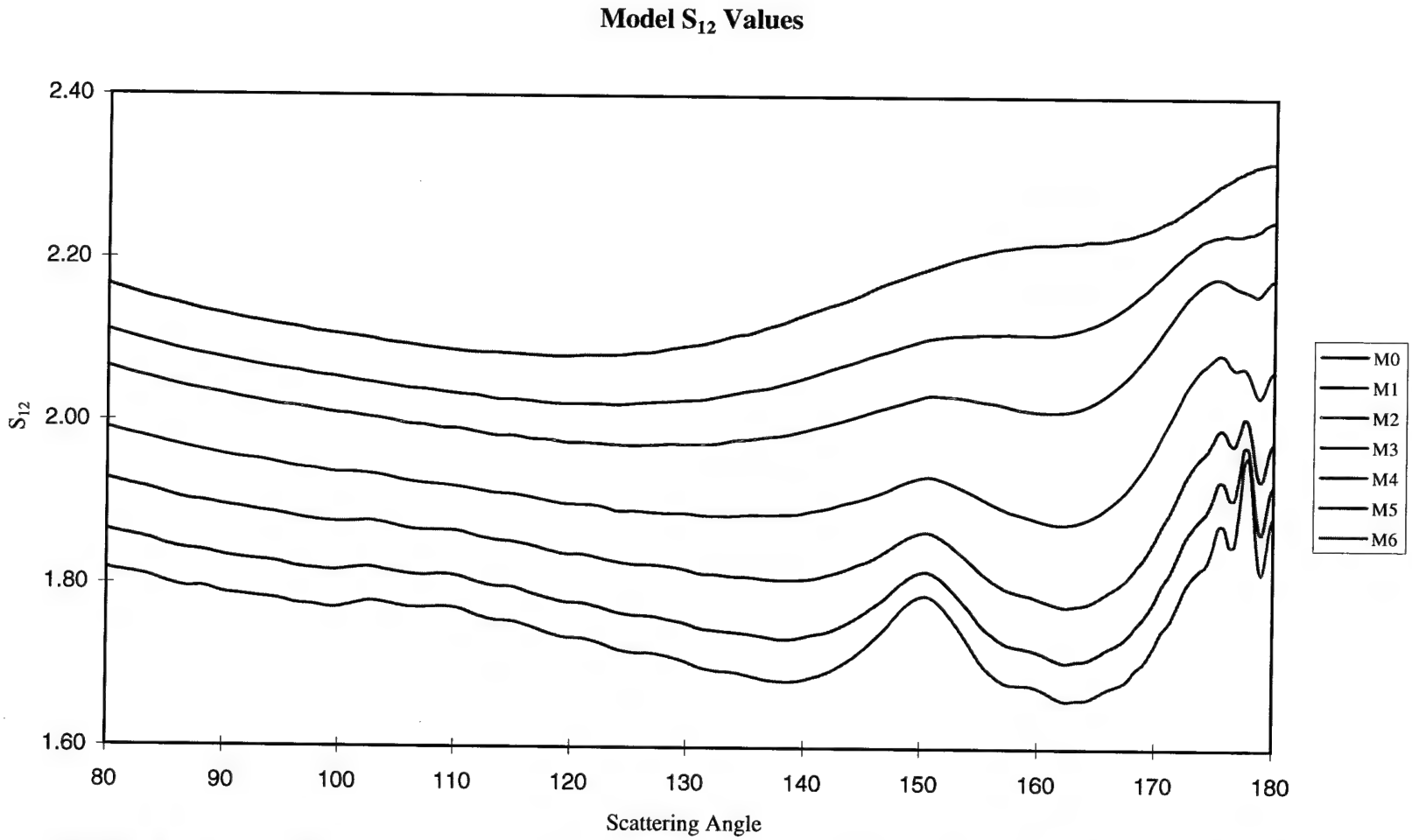

Figure 4.4. Model S_{12} Values. M0-M6 correspond to model two-mode, lognormal aerosol distributions with M0 representing the background (continental) aerosol mode and M6 representing the largest oceanic aerosol mode. S_{12} values are calculated using linearized, single-scattering theory (From Brown 1997).

V. RESULTS

A. VALIDATION

The satellite retrieval validation was accomplished by comparing the retrieval aerosol optical depth (AOD) output to sunphotometer AOD data collected during ACE-2. Five different instruments collected sunphotometer data at various times and places throughout the exercise period. The sunphotometer data used was correlated both spatially and temporally with the retrieved data to the greatest extent possible. Comparisons were made at 630 nm and 860 nm. In all cases the sunphotometer data was linearly interpolated to these wavelenghts. Only the NOAA-14 afternoon passes provided the proper sun-satellite geometry necessary to calculate AOD using this retrieval method. The uncertainty associated with the resolution of the satellite radiance measurements results in an average AOD uncertainty of ± 0.02 based on Brown (1997). The resultant data set can be seen in Table 5.1.

A CMEL Electronique 318A sunphotometer, operated by AERONET, was located at the Tenerife ground station. This station was located near Punta del Hidalgo at 28° N 16.6° W and an elevation of 10 m. Retrieved AOD data from the nearest pixel just off the coast from this ground station was used in the comparison. The sunphotometer data set was prescreened for clouds by AERONET. Eight matches to retrieved AOD data were found between 30 June and 18 July. The time difference between retrieved values and sunphotometer values ranged between zero and 39 min. An error of ± 0.01 is associated with the AOD measured by this instrument (Holben 1998).

date	time sr	AOD63 sr	AOD86 sr	time sp	AOD63 sp	AOD86 sp	source	Δt
30-Jun	1520	0.06	0.06	1509	0.079	0.061	TENERIFE	0011
1-Jul	1509	0.06	0.05	1509	0.056	0.037	TENERIFE	0000
7-Jul	1545	0.23	0.18	1525	0.197	0.167	TENERIFE	0020
8-Jul	1533	0.32	0.27	1555	0.345	0.308	TENERIFE	0022
10-Jul	1511	0.14	0.14	1456	0.119	0.105	TENERIFE	0045
17-Jul	1535	0.36	0.29	1541	0.401	0.371	TENERIFE	0006
18-Jul	1524	0.21	0.198	1527	0.222	0.194	TENERIFE	0003
16-Jul	1547	0.15	0.12	1626	0.118	0.108	TENERIFE	0039
21-Jun	1518	0.074	0.074	1510	0.059	0.054	AATS14	0008
10-Jul	1511	0.18	0.147	1459	0.132	0.104	AATS14	0012
17-Jul	1535	0.368	0.285	1607	0.375	0.354	AATS14	0032
24-Jun	1445	0.13	0.11	1445	0.13	0.095	AATS6	0000
25-Jun	1434	0.1	0.08	1434	0.127	0.078	AATS6	0000
10-Jul	1511	0.177	0.156	1450	0.17	0.125	AATS6	0021
11-Jul	1500	0.07	0.03	1512	0.057	0.038	UVISIR1 SAGRES	0012
12-Jul	1449	0.14	0.1	1456	0.129	0.115	UVISIR1 SAGRES	0007
22-Jun	1507	0.08	0.06	1508	0.078	0.053	IRRAD SAGRES	0001
23-Jun	1456	0.076	0.066	1454	0.066	0.06	IRRAD SAGRES	0002
24-Jun	1445	0.06	0.05	1447	0.055	0.037	IRRAD SAGRES	0002
30-Jun	1520	0.12	0.08	1517	0.07	0.026	IRRAD SAGRES	0003
10-Jul	1511	0.22	0.13	1513	0.166	0.122	IRRAD SAGRES	0002
11-Jul	1500	0.07	0.03	1459	0.065	0.065	IRRAD SAGRES	0001
12-Jul	1449	0.14	0.1	1450	0.14	0.091	IRRAD SAGRES	0001

Table 5.1. Validation data set, sr is the satellite retrieval data and sp is the sunphotometer data.

The ground station at Sagres, Portugal was located at the coastal military base Radio Naval de Sagres, 37° N 8.9° W and elevation 50 m. Two sunphotometers, UVISIR-1 and IR-RAD, were operated at this station by FISBAT. Retrieved AOD data from the nearest pixel just off the coast from this ground station was used in the comparison. Two matches to retrieved AOD were found for the 11 and 12 July data from the UVISIR-1 instrument. Seven matches to the retrieved AOD data were found between 22 June and 12 July from the IR-RAD instrument. Errors for the data collected by the two sunphotometers at this station were not available, but were assumed to be similar to the error reported for the other

instruments used during the exercise and assigned a value of ± 0.01.

NASA Ames operated the AATS-6 aboard the R/V Vodyanitsky. The ship spent most of its underway time south of Sagres outside the Strait of Gibraltar, but in one coordinated experiment the ship traveled farther south off the coast of Morocco. AOD values from this sunphotometer were screened for clouds and ship mast interference. Two matches were found, one on 24 June and one on 25 June, during the time when the ship was outside the Strait of Gibraltar (35.6° N 9.2° W and 36.1° N 9.0° W respectively). The temporal agreement in these cases is good. One match was found for 10 July when the ship was off the coast of Morocco (29.3° N 11.9° W). There is a 21 min. difference in the data times for this match, but this is considered acceptable since the ship moves a very short distance and the aerosol loading can be assumed to be consistent over this time. The error associated with the AATS-6 AOD values are between ± 0.006 and ± 0.008.

The AATS-14 was flown aboard the CIRPAS Pelican aircraft. The majority of flights were in clear air masses nearby the Island of Tenerife, but one flight was near the coast of Morocco in order to coordinate with ship measurements. The aircraft flew at many altitudes due to the requirement of other instrumentation onboard. The AOD values used for comparison were only those calculated when the plane was at an altitude of 100 m or less and near the time of the satellite retrieval. For this short period of time (6 min or less) the AOD values were averaged and the average was used as a single value for comparison. Three matches were found for this data set: 21 June near 28.9° N 17.2° W had a temporal difference of less than 11 min, 10 July near 29° N 11.13° W had a temporal difference of less

than 13 min, and 17 July near 27.8° N 16.6° W had a temporal difference of less than 34 min. The error associated with the AATS-6 AOD values are between ± 0.004 and ± 0.008.

Some retrieved AOD data was not used even though there was matches to sunphotometer data. In areas contaminated by sun glint or clouds, retrieved AOD values were automatically throw away by the retrieval process. AOD values that were near the edge of the satellite pass (defined by 100 pixels in the composite process) were not considered valid. Finally, retrieved values that had valid sunphotometer matches but were in a strong gradient of AOD were not used. Strong gradients of retrieved AOD, doubling or tripling of the AOD value over a few pixels, are suspect for matches because they may be inconsistent both spatially and temporally with the sunphotometer AOD and it is difficult to place the match within the gradient.

The scattering angle used in the calculation of retrieved AOD was checked to ensure there was no bias to a single angle when choosing a value for the phase function. As seen in figures 4.2 and 4.3 the value of the phase function converges near a scattering angle of 140°. Data with scattering angles near 140° are not affected by aerosol model type and would therefore not provide a robust validation. The range of scattering angles for this data set is between 152° and 176° which is in an area of significant spreading of modeled phase function values.

The resultant data set is shown in a scatter plot in Figure 5.1 and indicates a positive validation of the retrieval method. Sunphotometer source and wavelength data points are grouped together in the plot. There is very good agreement in the lower optical depth range for all sources and both wavelengths. In the higher optical depth range the correlation is slightly off, more so for the values at

860 nm. Since these high AOD values are primarily due to dust aerosol, the bias may be due to the non-absorbing aerosol assumption made in the satellite retrieval method. If aerosol absorption was included the retrieved AOD values would be higher and correlate more closely with the sunphotometer AOD. Dust aerosols typically have single scatter albedo values of 0.9 or less (Ignatov *et al.*, 1995). Even with this problem the correlation coefficient has a value of 0.88. Additionally, the standard error for the 630 nm and 860 nm data set is 0.023 and 0.022 respectively. Brown (1997) using data from TARFOX, also achieved a positive validation of this AOD retrieval method. The validation of the AOD retrieval method is assumed for the ACE-1 composites discussed below.

Another validation method used by Nakajima and Higurashi (1998) compares the Ångström exponent calculated from satellite retrieved AOD with those calculated from sunphotometer AOD. A scatter plot of the Ångström exponents calculated from the ACE-2 data set is given in Figure 5.2. There is good agreement between the calculated values with the exception of a few outliers. The outliers are all points from the Sagres data set and all had extremely low values of AOD at both 630 nm and 860 nm. Optical depth values this low are calculated from radiances near the detection limit for AVHRR where the magnitude of AOD is about the same as the uncertainty due to digitization of the radiance. This can lead to anomalously high or low ratios of AOD and therefore anomalous values of the Ångström exponent. The two outliers in the upper left of figure 5.2 are both from 11 July and both have high satellite retrieved AOD ratios compared to the sunphotometer ratios (see Table 5.1 for data values). The third outlier, on the right side of Figure 5.2, is from 30 June. The satellite retrieved AOD are slightly higher than the sunphotometer AOD, but their

relative difference is similar. Since the AOD values are low the ratio of the sunphotometer AOD values produces a higher Ångström exponent. The standard error of this data set with the outliers is 0.73 and without the outliers is 0.41. This adds to the confidence of our validation.

B. REGIONAL ANALYSIS

The regional composite images can been seen in figures 5.3-5.7. The composites cover larger areas than the actual exercise areas in order to identify possible sources and transport of aerosols. Figures 5.3 and 5.4 (a)-(c) are images of AOD, at 630 nm and 860 nm respectively, for the three exercise areas. Figures 5.5(a)-(c) are composite images of AOD ratio. The ratio of AOD at two different wavelengths is related to the Ångström exponent and is an indicator of aerosol size distribution. Higher Ångström exponent values indicate areas of pollution or biomass burning and lower values indicate marine and dust aerosols (Nakajima and Higurashi, 1998). Figures 5.6(a)-(c) are images of the standard deviation for AOD at 630 nm. These images are used to indicate the consistency of the aerosol properties over the exercise period. The number of pixels per bin that were used in the composites is shown in figures 5.7(a)-(c). Higher numbers correlate to areas which where generally cloud free and not affected by sun glint. Numbers above 100 represent a contribution a more than one satellite pass used in the composite. The statistics cited below are for the exercise areas only. A white box on the images in figures 5.3(a)-(c) indicate the exercise areas.

1. ACE-1

The ACE-1 study area, defined by research aircraft and ship operations, was between 40°-55°S and 135°-160°E. During

the field operations period there was an above average occurrence of cold frontal passage. A long wave trough passed over the exercise area during the course of the experiment. This led to strong westerly to northwesterly flow in November and southerly to southwesterly flow in December. Sea salts dominate aerosol properties in this area (Hainsworth *et al.*, 1998). As expected the AOD calculated (figures 5.3(a) and 5.4(a)) were low over most of the area with a mean of 0.13 at 630 nm and 0.11 at 860 nm. This is consistent with the assumption that continental aerosols are not the primary influence in this area. There are some areas of higher AOD over the southern ocean near the sub-tropical convergence zone. This may be due to increased wave action and therefore higher surface reflection contamination in the retrieval. Additionally, this area is also known to be a large producer of non-sea salt sulfates that contribute to aerosol concentrations and may lead to higher AOD. Individual images of retrieved AOD from early in the exercise period revealed higher AOD off the East Coast of Australia consistent with continental aerosols being advected by the observed westerly winds. Some high AOD ratio values (figure 5.5(a)) are scattered over the eastern portion of the composite. This may indicate an influx of anthropogenic aerosols into this area or an abundance of biologically produced sulfate aerosols. The standard deviation of retrieved AOD (figure 5.6(a)) is low with a mean of 0.028 at 630 nm and 0.064 at 860 nm. This is indicative of the relatively homogenous aerosol properties in this area.

2. TARFOX

TARFOX was conducted in the continentally influenced environment off the East Coast of the United States near

Wallops Island, Virginia. A variety of aerosol conditions, from relatively clean to moderately polluted, were observed. A persistent upper-level trough created extensive cloudiness on many days and highly variable haze conditions due to frequent shortwave weather systems passing over the area. Additionally, Hurricane Bertha threatened the exercise area for three days. The TARFOX composites extend south and west in order to identify aerosol sources from sub-tropical latitudes and aerosol transport across the North Atlantic Ocean. AOD composites are shown in figures 5.3(b) and 5.4(b). The mean values from these composites are 0.353 at 630 nm and .271 at 860 nm. These higher values are consistent with continental soil and pollution aerosols. Another source is mineral dust that originates in North Africa. This dust makes it way across the sub-tropical North Atlantic Ocean to the Caribbean where it gets entrained in the mid-latitude westerly flow. This process is evident in the composite images. Extensive cloudiness may bias the retrieved AOD. The cloud screen algorithm has difficulty near cloud boundaries and it is in these areas that aerosol humidification may cause higher calculated values of AOD. The AOD ratio (figure 5.5(b) is high near areas where pollution aerosols are expected, specifically off the coast of major cities in the North East U. S. This feature, due mainly to the increased amount of small aerosol particles from combustion processes, persists well into the North Atlantic Ocean. The mean values of AOD standard deviation for this region were 0.148 at 630 nm and 0.112 at 860 nm. The relatively high standard deviation of AOD (figure 5.6(b)) is indicative of the variability of the aerosol conditions associated with this region.

3. ACE-2

The ACE-2 area was selected based on its exposure to various aerosol types, including clean marine, anthropogenic from Europe and desert dust. The main study area was between 23°-44°N and 8°-25°W. The composite area extends further west into the North Atlantic Ocean and east into the Western Mediterranean Sea. The mean AOD values are 0.142 at 630 nm and 0.126 at 860 nm. This is consistent with most of the area being dominated by clean marine aerosol. The most significant feature is the long plume of high AOD that extend off the African continent into the North Atlantic Ocean (see figures 5.3(c) and 5.4(c)). AOD values approaching 1.0 are common in this plume. An anomalous area of high AOD is present in the northwest corner of the composite. This may be an extension of the dust plume that has been caught in the mid-latitude westerlies or aerosols that made there way from the Western Atlantic around the sub-tropical high. AOD Plumes extending off the coast of Algeria and Tunisia into the Mediterranean Sea are associated with dust carried by Sirocco winds. There is some evidence of pollution out breaks, based on higher AOD, south and west of Portugal. These events are seen periodically in individual cases, but are averaged out over time in the composite. The mean standard deviation of AOD was 0.064 at 630 nm and 0.061 at 860 nm. The AOD ratio (figure 5.5 (c)) is low and fairly consistent over the entire area. North of the dust plume the ratio values increase which may be a result of pollution aerosols from the European continent. The mean standard deviations are biased by large standard deviation values in the area of the African dust plume (see figure 5.6(c)).

A scatter plot of Ångström exponent versus AOD is useful for an optical characterization of aerosols in terms

of the typical particle size and distribution. The typical observed value of the Ångström exponent is approximately 1 for small urban-type aerosols and approximately 0 for large soil-derived particles (Nakajima and Higurashi, 1998). Figure 5.8 is a scatter plot of Ångström exponent vs. AOD for the ACE-2 data set. The Sagres and AATS-6 data points tend to have higher Ångström exponents, although lower AOD, as is expected due to urban-aerosol effects from the European continent. The AERONET and AATS-14 data points tend to have lower Ångström exponents, with varying AOD, as is expected in the open ocean near the African dust plume. The satellite data points correlate well with the respective sunphotometer data points.

4. Regional Comparison

Regional comparison is accomplished through frequency plots of AOD at 630 nm and 860 nm wavelenghts (figure 5.9). The data used in the histogram is limited to only the operational areas of each exercise as described above. The histogram plots for ACE-1 and ACE-2 have a similar profile with modes of 0.115 and 0.095 (at 630 nm) respectively. This is indicative of the relatively clean environment in these regions. The effect of the African dust plume in ACE-2 can be identified by the tail of the histogram plot toward higher values of AOD. It is interesting that the ACE-2 frequency plot has a lower mode than the ACE-1 plot even though the mean AOD in the ACE-1 composite is larger. This is a good example of regional differences in aerosol distributions. The ACE-1 area is influenced by essentially one type of aerosol constituent that leads to a similar mode and mean. The ACE-2 area has several aerosol constituents. The main constituent at the dominant mode is similar to ACE-1, but its lower mode value implies smaller particles. The other constituents, dust and anthropogenic aerosols,

contaminate the area and lead to the higher average AOD. The TARFOX plot has a much higher mode (0.185 at 630 nm) and a significantly larger spread. This is indicative of the larger aerosol loading and varied aerosol types in this region.

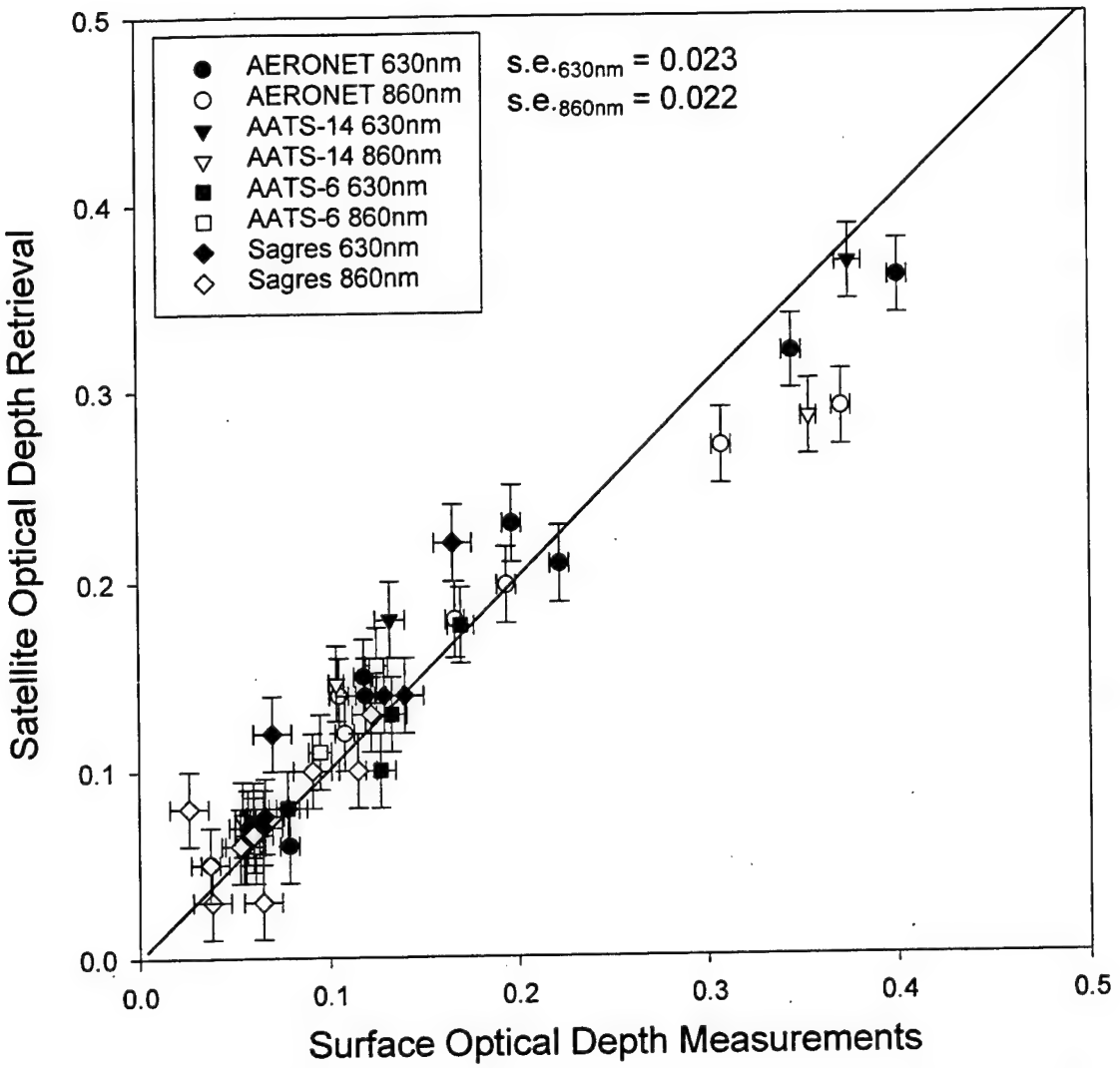

Figure 5.1. Scatter diagram of surface measured aerosol optical depth versus aerosol optical depths retrieved from satellite. The correlation is very strong and the standard error is low. Absorption by aerosols is considered to be zero in the retrieval method. This may account for the weaker correlation at higher values of optical depth.

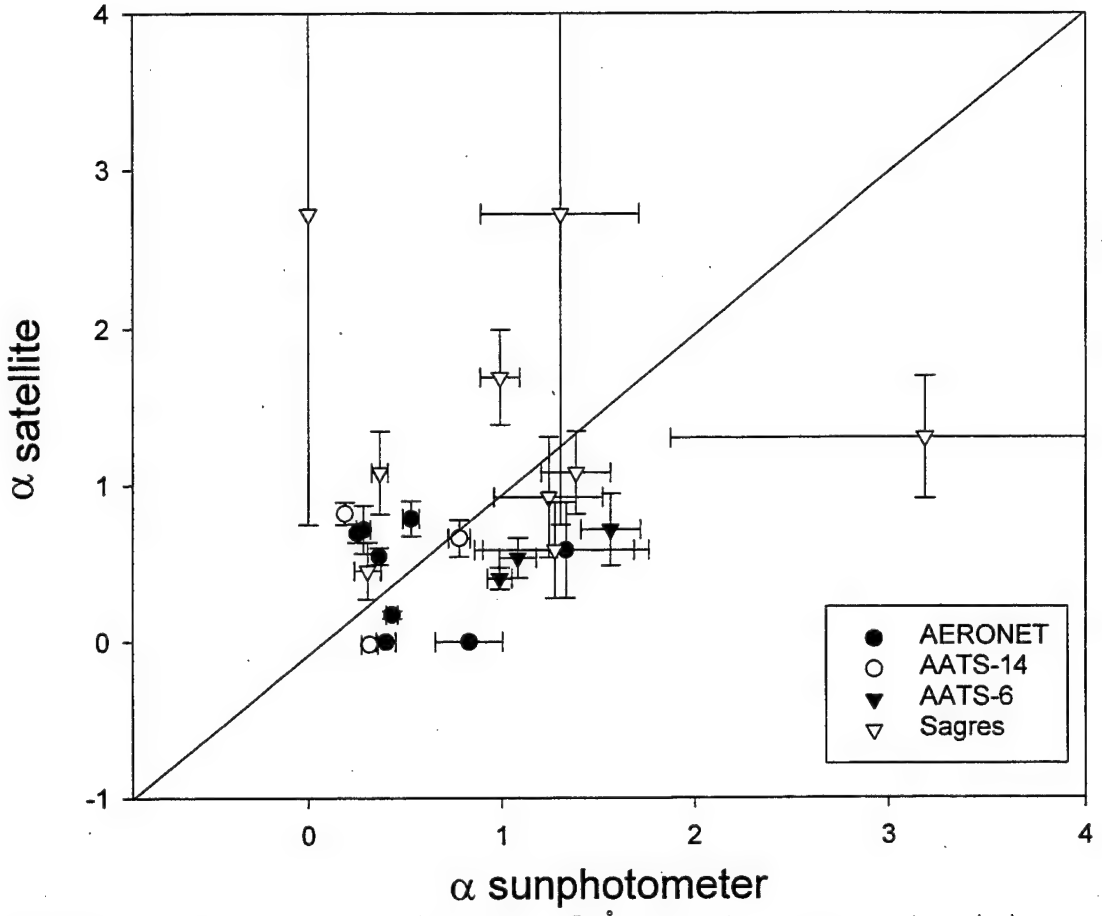

Figure 5.2. Scatter diagram of Ångström exponents (α) calculated from sunphotometer AOD vs satellite retrieved AOD. There is good agreement between the two data sets for low values of α. Small values of α indicate an area of soil-derived particles such as the ocean area next to the Sahara desert (Nakajima and Higurashi, 1998). The few outliers that are present are due to low values of AOD at these points which leads to a higher error. The standard error for this data is 0.73 with the outliers and 0.41 without the outliers.

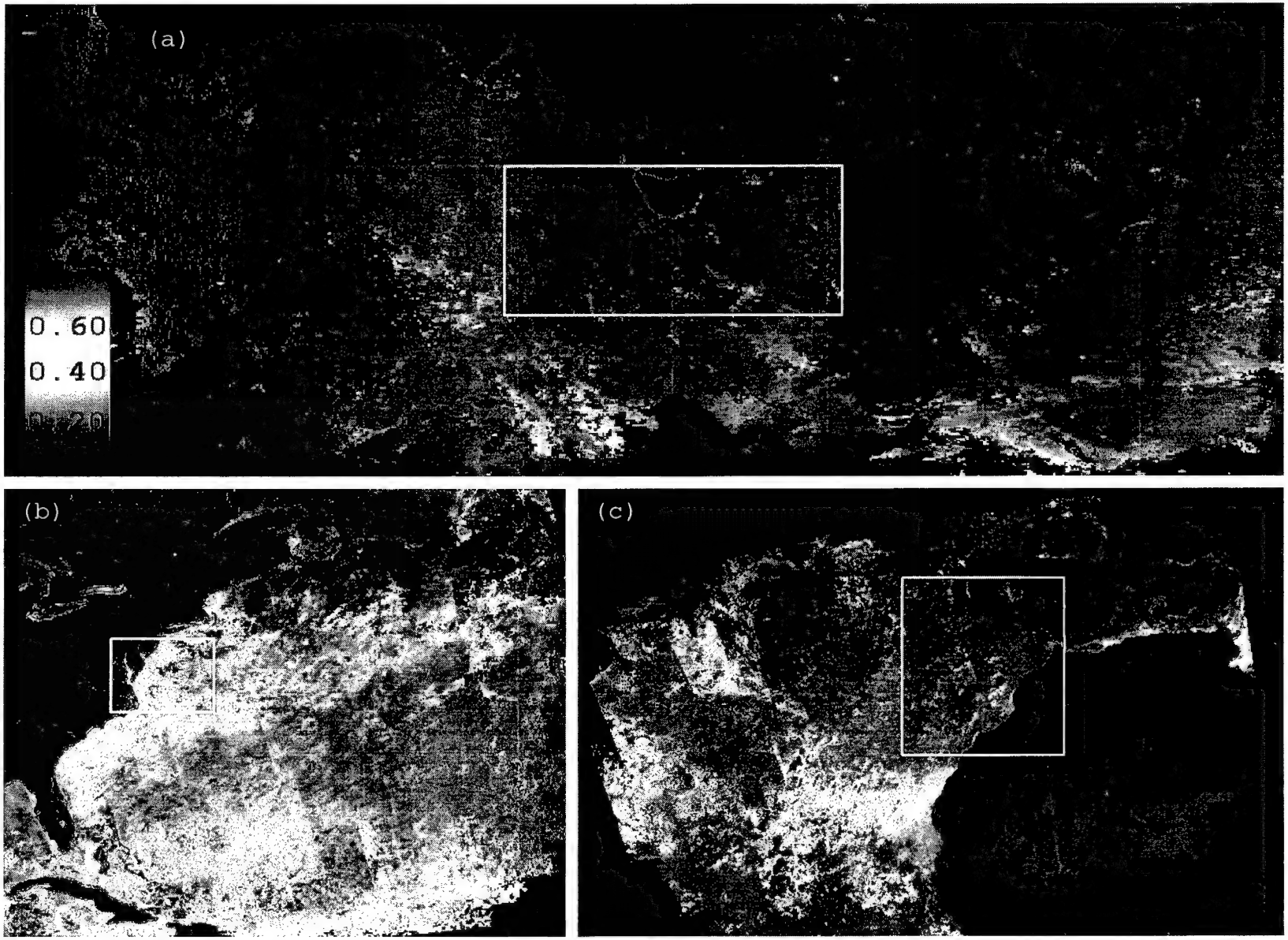

Figure 5.3. AOD composite (630nm) (a) ACE-1 (b) TARFOX (C) ACE-2.

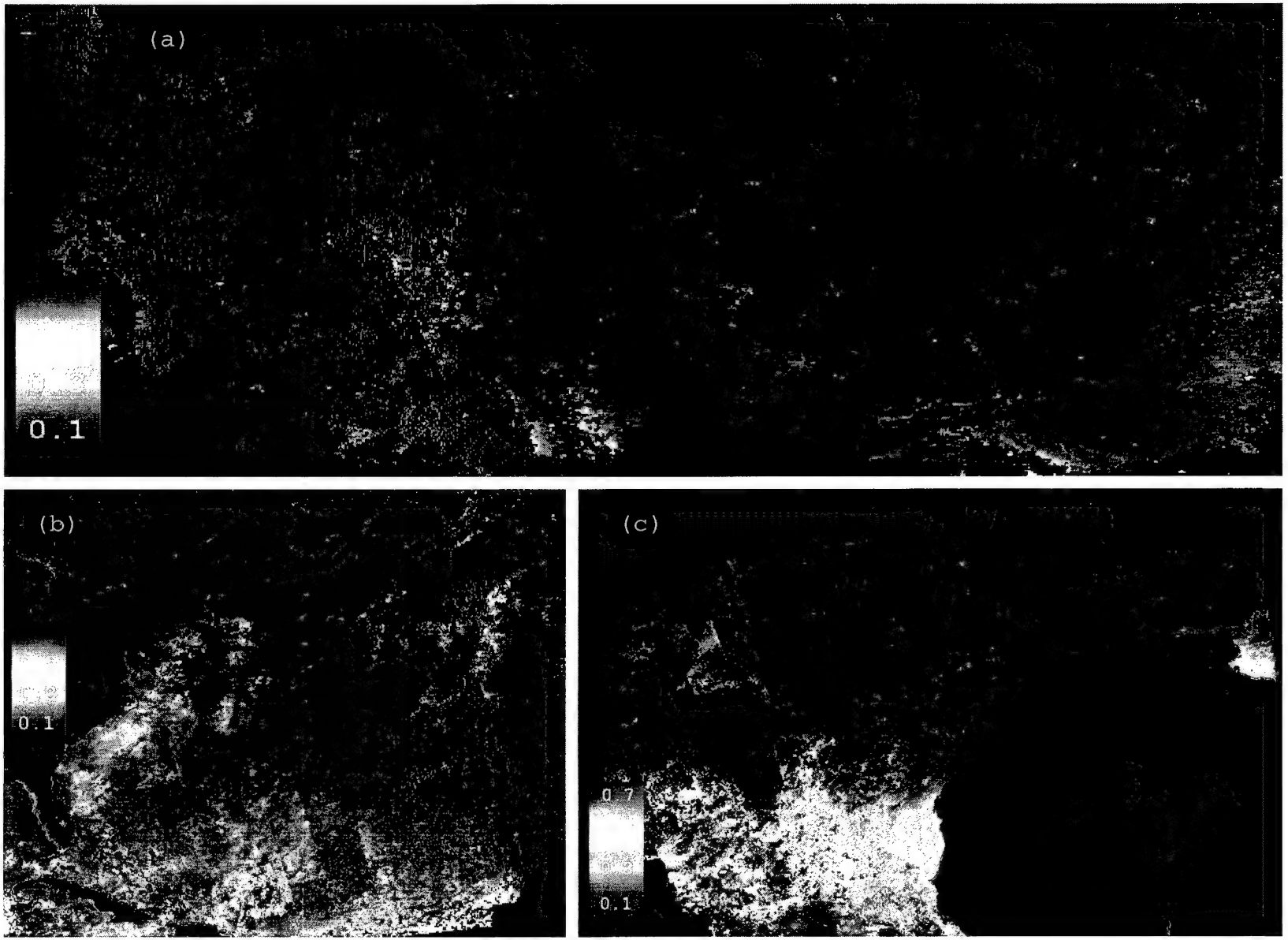

Figure 5.4. AOD composite (860nm) (a) ACE-1 (b) TARFOX (C) ACE-2.

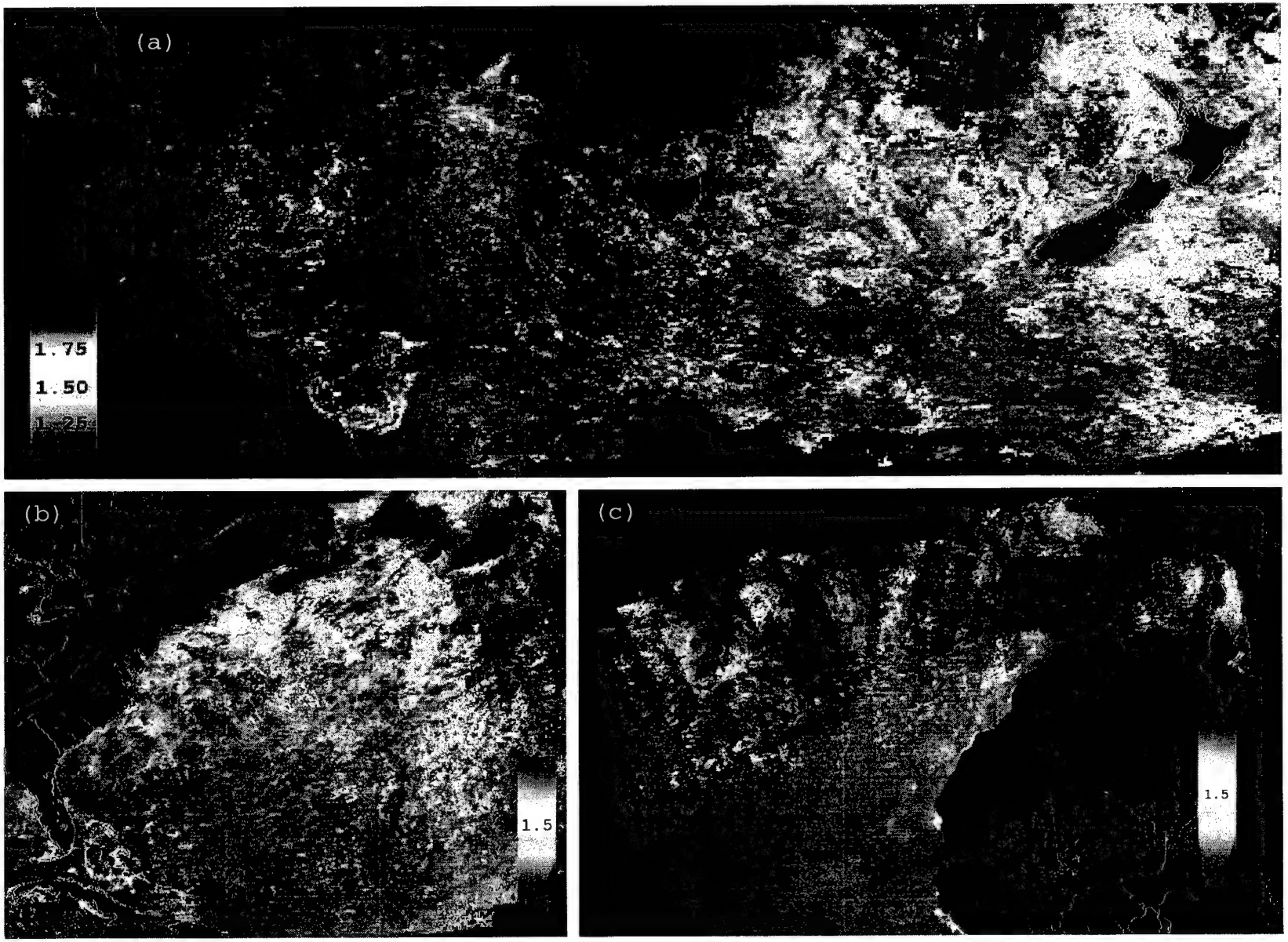

Figure 5.5. AOD ratio composite (630nm/860nm) (a) ACE-1 (b) TARFOX (C) ACE-2.

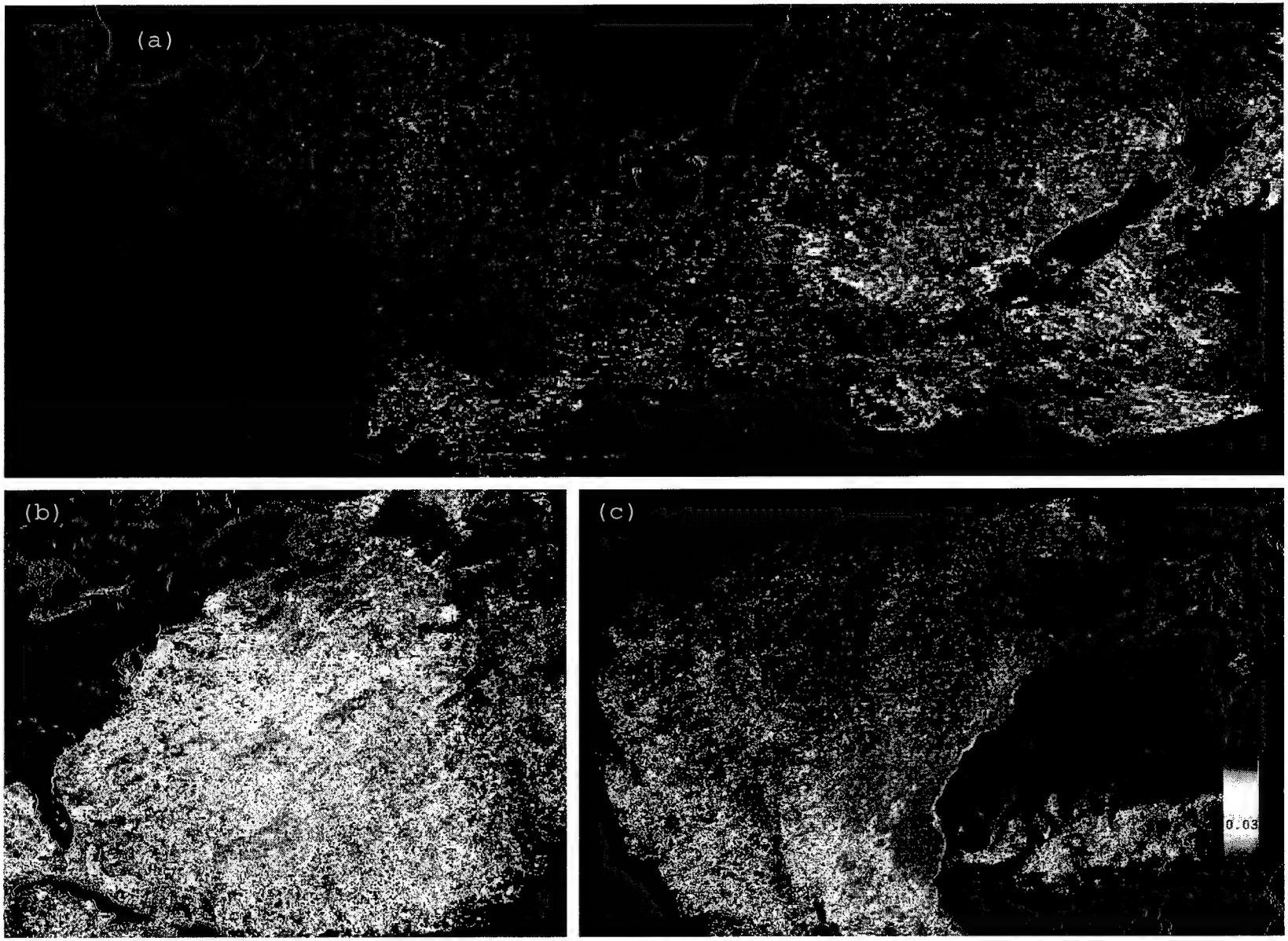

Figure 5.6. AOD standard deviation composite (630nm) (a) ACE-1 (b) TARFOX (C) ACE-2.

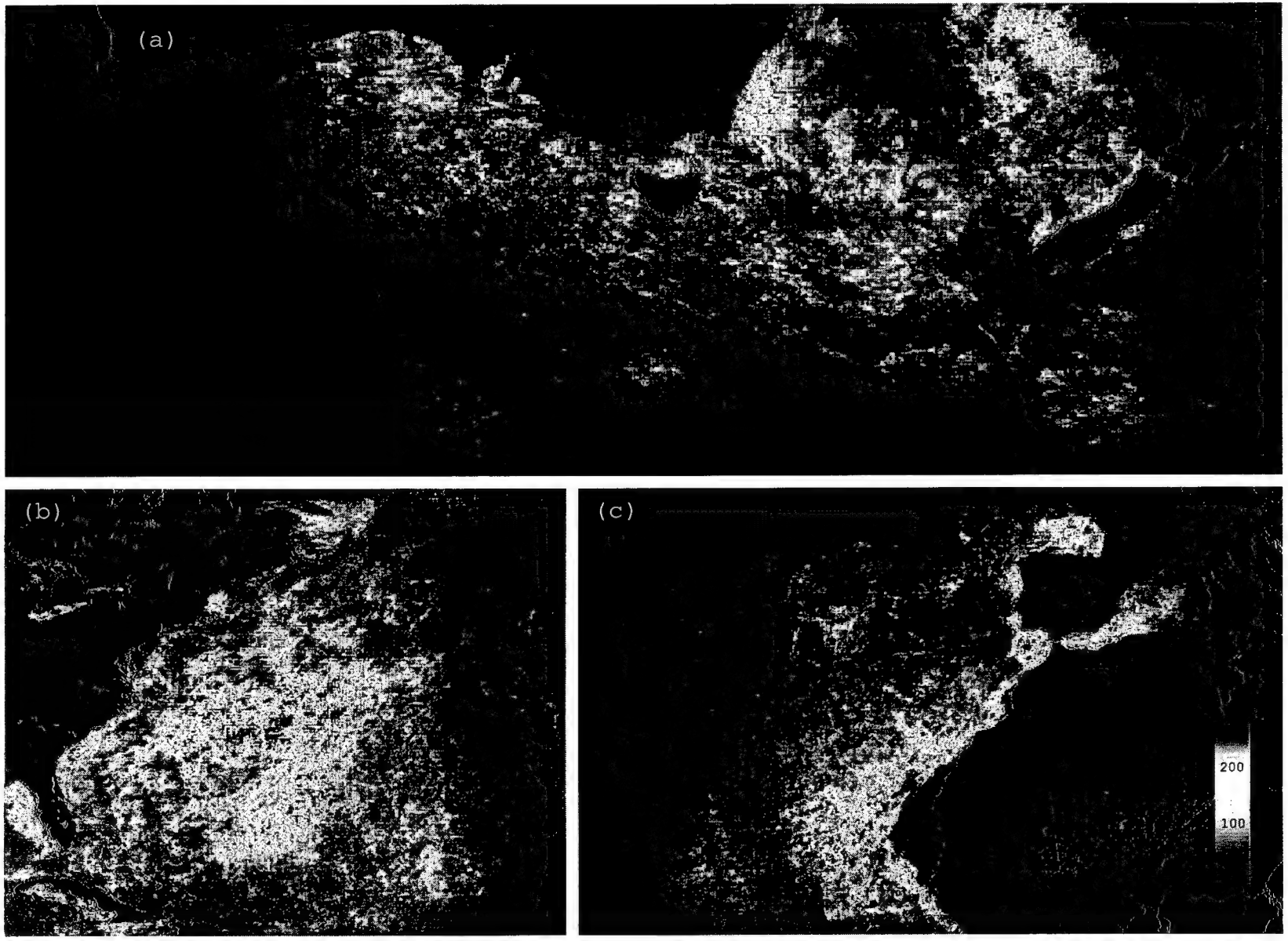

Figure 5.7. AOD observations per bin (630nm) (a) ACE-1 (b) TARFOX (C) ACE-2.

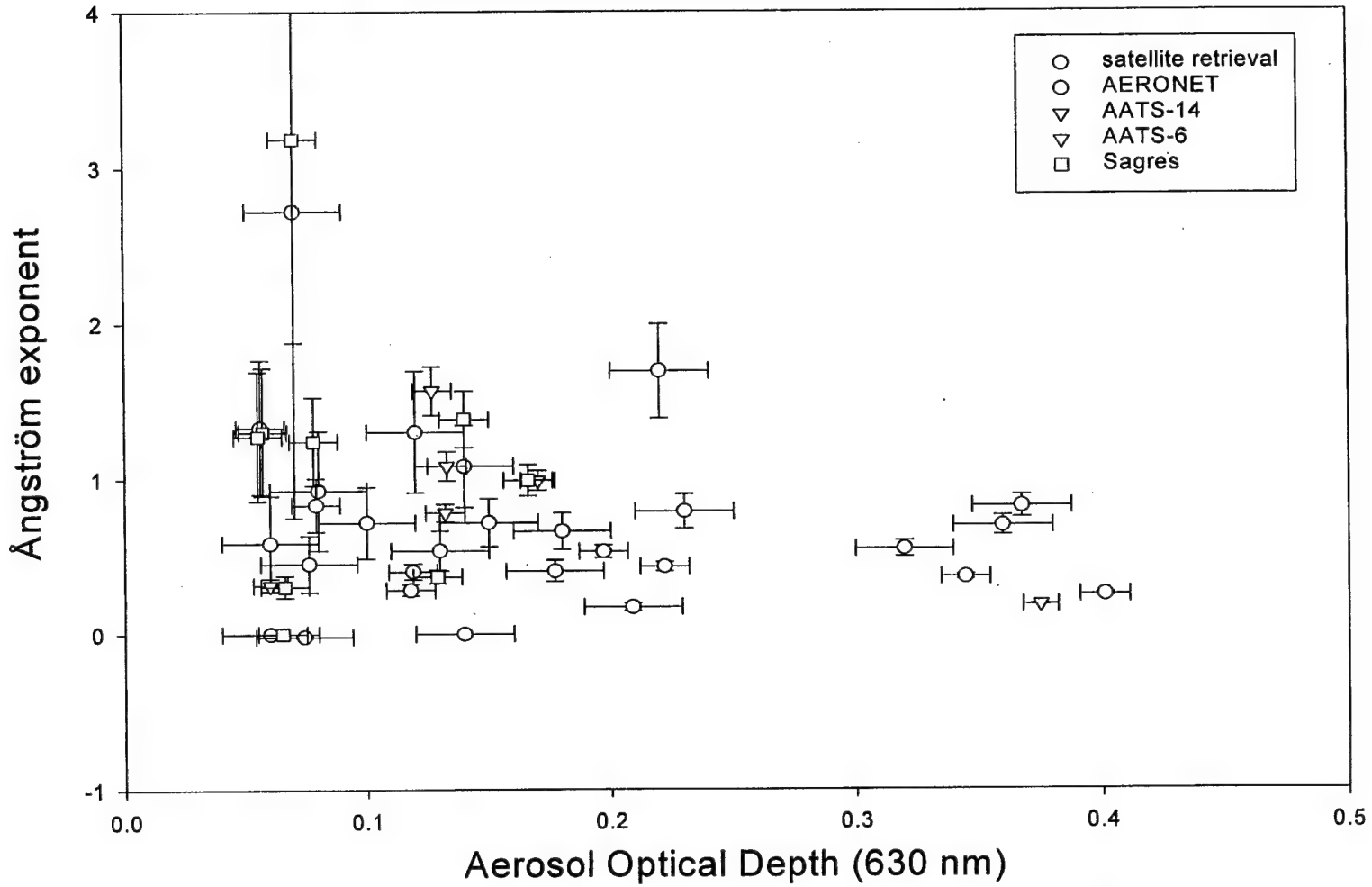

Figure 5.8. Scatter diagram of Ångström exponent vs. AOD at 630 nm.

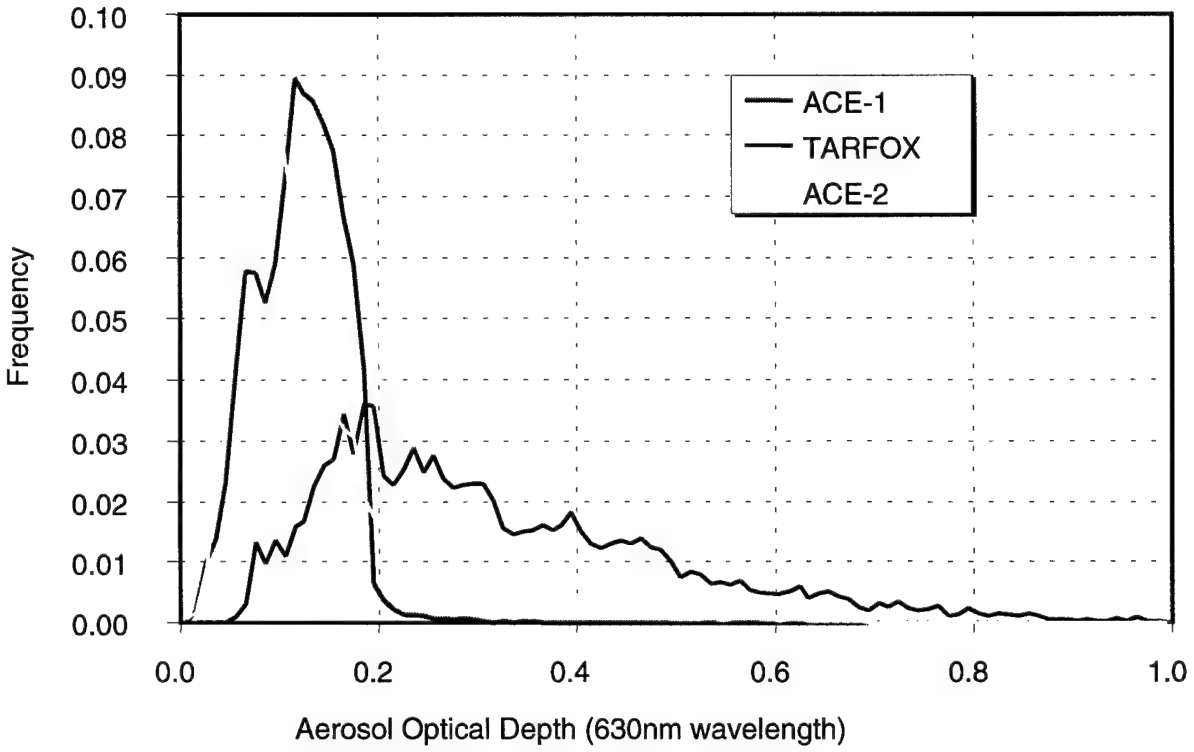

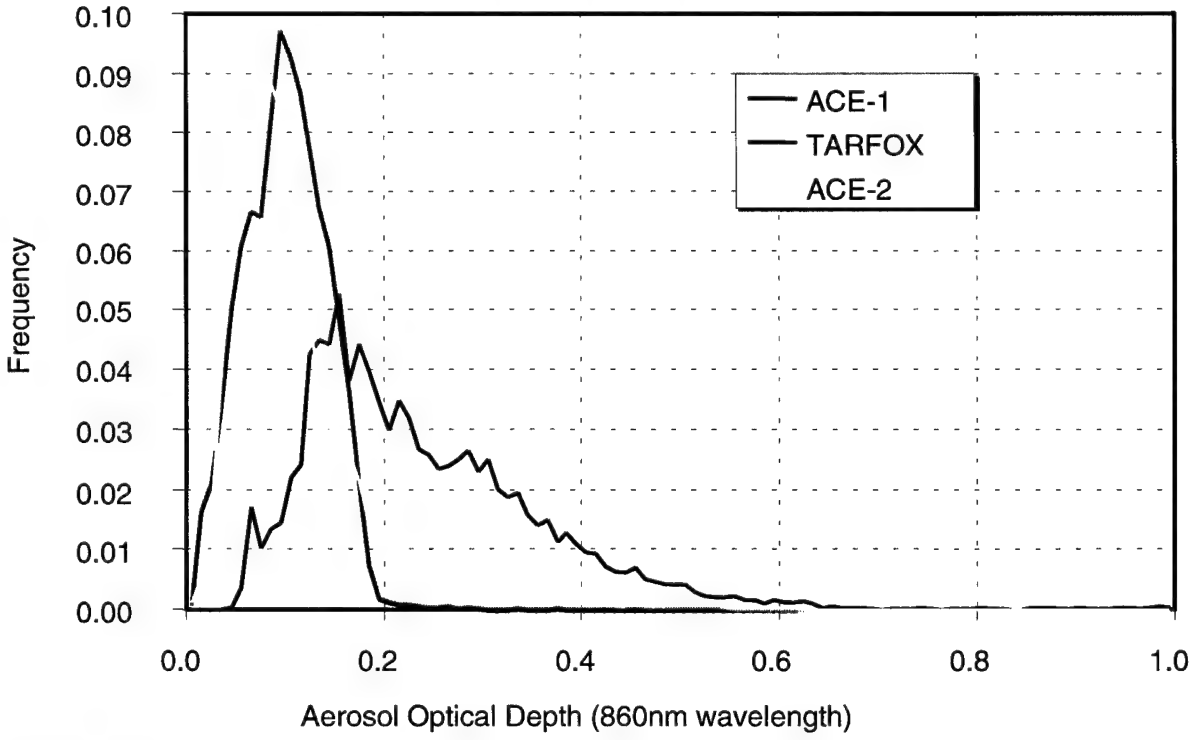

Figure 5.9. Histograms of aerosol optical depth at 630 nm and 860 nm for ACE-1, TARFOX and ACE-2.

VI. CONCLUSIONS/RECOMMENDATIONS

A. CONCLUSIONS

A radiative transfer algorithm in the solar wavelengths for the NOAA POES AVHRR is presented for the cloud-free, marine atmosphere. This algorithm combines linearized, single-scattering theory with an estimate of bi-directional surface reflectance. Phase functions are parameterized using an aerosol distribution model and the ratio of radiance values measured in channels 1 and 2 of the AVHRR. The aerosol distribution model is based on a bimodal lognormal distribution with significant modes at 0.1 and 0.3 μm. Ratios of channel 1 to channel 2 are crossed with the scattering angle in a look-up table (LUT) to determine the best representative aerosol distribution. Using this model and, again, the scattering angle the phase function is chosen from a LUT calculated from Mie theory. Automated cloud screening is accomplished through preset thresholds and known comparisons using AVHRR channels 2-5 based on Saunders and Kriebel, 1988. Sun glint removal is based on Cox and Munk (1954) and takes into account sun-satellite geometry and wind speed.

Retrieved satellite aerosol optical depth (AOD) was compared to surface measured sunphotometer AOD collected during the International Global Atmospheric Chemistry (IGAC) Project's Second Aerosol Characterization Experiment (ACE-2) from June 16 to July 25, 1997. Sunphotometer data from four independent sites were used in the comparison, ground stations at Tenerife Island and Sagres, Portugal, AATS-6 on board the R/V Vodyanitskiy, and AATS-14 on board the CIRPAS aircraft Pelican. There was very good agreement between the AOD retrieved from satellite and those measured by

sunphotometer, especially at low values of AOD. At higher values of AOD the retrieved values are low, but this is most probably due to the no-absorption assumption made in the retrieval. The comparison data set has a correlation coefficient of 0.88 with a standard error of 0.02 at both channel 1 and 2 wavelengths. This indicates a positive validation of the retrieval method. Another validation method, used by Nakajima and Higurashi, 1998, compares Ångström exponents calculated from the data set. A similar comparison done here shows good agreement between the retrieval AOD and the surface measured AOD. This adds to the positive validation. Validation of this retrieval technique was also seen in Brown (1997) using data from TARFOX. The retrieval technique is assumed to validate for the ACE-1 area and is used for the regional analysis discussed below.

Regional aerosol properties are examined with an emphasis on the differences between the ACE-1, TARFOX and ACE-2 regions. AOD determined from satellite retrieval were averaged for the duration of the exercise periods and combined into composite images at 10X10 km resolution. Statistics were also calculated for each exercise area. The images give a good indication of aerosol loading as well as source and transport regions in each area. A scatter plot of AOD versus Ångström exponent for the ACE-2 data set is used to examine aerosol characteristics. Data from Sagres and R/V Vodyanitskiy have higher Ångström exponents and lower AOD consistent with urban-type aerosols. Data from Tenerife and Pelican have lower Ångström exponents and a varying AOD consistent with dust aerosol influence. AOD frequency plots are used to identify region differences of the three exercises. ACE-1 and ACE-2 regions have strong modes at AOD at around 0.1, but ACE-2 tails toward higher values consistent with urban and dust aerosol intrusion.

The TARFOX region has a noticeable mode at AOD around 0.2, but has significant spread of AOD values consistent with the varied aerosol constituents in that area.

B. RECOMMENDATIONS

As a result of this study, the following recommendations are suggested:

-Continue satellite retrieval validation with additional quality controlled data from these exercises, as well as future exercises. *In situ* data from ACE-1, TARFOX, and ACE-2 that have been well verified are increasingly becoming more available. ACE-Asia, which will be conducted off the west coast of Asia near Japan in 2000-2002 will provide additional regional information. This validation should include tests of individual components of the retrieval such as parameterization of the phase function, water vapor corrections, etc.

- Assess the aerosol distribution model to see if a better fit can be obtained based on known aerosol distributions. Based on this and other recent studies the modes and standard deviations for the log-normal aerosol distribution can be tuned to specific regions or expected aerosol types.

-Extend the S_{12} phase function parameterization technique to the next generation AVHRR with 1.6 μm daytime channel. This wavelength is less sensitive to water vapor the the current channel 2.

-Continue to improve on cloud screen analysis using more sophisticated techniques. Tests with static threshold values can be replaced with tests that determine thresholds dynamically from detected radiances. Thresholds can also be set by numerical model output such as for SST.

-Improve sun glint removal process by incorporating real-time wind speed analysis. Wind speed as well as wave and swell direction can be obtained from other satellite sensors or from numerical models to get a more accurate sun glint approximation.

LIST OF REFERENCES

Bates, T. S., B. J. Huebert, J. L. Gras, F. B. Griffiths, P. A. Durkee (1998). International Global Atmospheric Chemistry (IGAC) Project's First Aerosol Characterization Experiment (ACE 1): Overview. *J. Geophys. Res.*, **103,** 16297-16318.

Brown, B. B. (1997). Remote measurement of aerosol optical properties using the NOAA POES AVHRR and GOES imager during TARFOX. M.S. Thesis, Naval Postgraduate School, Monterey, CA, 73pp.

Charlson, R. J., , S. E. Swartz, J. M. Hales, R. D. Cess, J. A. Coakley, Jr., J. E. Hansen and D. J. Hoffman (1992). Climate forcing by anthropogenic aerosols. *Science*, **255**, 423-430.

Cox, C., and W. Munk (1954). Measurements of the roughness of the sea surface from photographs of the sun's glitter. *J. Opt. Soc. Am.*, **44,** 838-850.

Dalu, G. (1986). Satellite remote sensing of atmospheric water vapor. *Int. J. Rem. Sen.*, **7**, 1089-1097.

Durkee, P. A., F. Pfeil, E. Frost and R. Shema (1991). Global analysis of aerosol particle characteristics. *Atmos. Env.*, **25A**, 2457-2471.

Elterman, L. (1970). *Vertical-attenuation model with eight surface meteorological ranges 2 to 13 kilometers.* AFCRL-70-0200 Air Force Cambridge Research Laboratory, Cambridge, MA, 56pp.

Gordon, H. R. and D. K. Clark (1980). Atmospheric effects in the remote sensing of phytoplankton pigments. *Boundary Layer Met.*, **18**, 299-313.

Hainsworth, A. H. W., A. L. Dick, and J. L. Gras (1998). Climatic context of the First Aerosol Characterization Experiment (ACE 1): A meteorological and chemical overview. *J. Geophys. Res.*, **103**, 16319-16340.

Holben, B. N., T. F. Eck, I. Slutsker, D. Tanre, J. P. Buis, A. Setzer, E. Vermote, J. A. Reagan, Y. J. Kaufman, T. Nakajima, F. Lavenu, I. Jankowiak, A. Smirnov (1998). AERONET-A federated instument network and data archive for aerosol characterization. *Rem. Sen. Env.*, **66**, 1-16.

Intergovernmental Panel on Climate Change (IPCC) (1996). Climate Change 1995, J. T. Houghton et al. (Eds.). Cambridge University Press, New York.

IGAC (1995). *International Global Atmospheric Chemistry Project, North Atlantic Aerosol Characterization Experiment (ACE-2). Radiative Forcing due to Anthropogenic Aerosols over the North Atlantic Region. Science and Implementation Plan.* European Commission DG XIII, Report No. CL-NA-16229-EN-C. 112pp.

Ignatov, A. M., L. L. Stowe, S. M. Sakerin and G. K. Korataev (1995). Validation of the NOAA/NESDIS satellite aerosol product over the North Atlantic in 1989. *J. Geophys. Res.*, **100**, 5123-5132.

Kidwell, K. B. (1995). *NOAA Polar Orbiter Data Users Guide.* National Environmental Satellite, Data, and Information Service (NESDIS), National Oceanic and Atmospheric Administration, 394pp.

Koepke, P. (1984). Effective reflectance of ocean whitecaps. *Appl. Opt.*, **23**. 1816-1824.

Liou, K. N. (1980). *An Introduction to Atmospheric Radiation.* Academic Press, New York, 392pp.

Livingston, J. M. and P. B. Russell (1997). Aerosol optical depth spectra, vertical profiles, and horizontal transects derived from TARFOX airborne sunphotometer measurements, EOS, *Trans. Amer. Geophys. Union*, **78**, S92.

Mahony, T. P. (1991). Water vapor influence on satellite-measured aerosol characteristics. M.S. Thesis, Naval Postgraduate School, Monterey, CA, 43pp.

Matsumoto, Y., C. Mina, P. B. Russell, and W. B. Vanark (1987). *Airborne tracking sunphotometer apparatus and system.* NASA Technical Report 1988005110 N (88N14492), NASA Ames Research Center, Moffett Field, CA, 10pp.

Nakajima, T. And A. Higurashi (1998). A use of two-channel radiances for aerosol characterization from space. *Geophys. Res. Let.*, **25,** 3815-3818.

Ramsey, R. C. (1968). *Study of the Remote Measurement of Ocean Color.* Final Report, TRW, NASW-1658, 94pp.

Rao, C. R. N. and J. Chen (1995). Inter-satellite calibration linkages for the visible channels of the Advanced Very High Resolution Radiometer on the NOAA-7, -9, and -11. *Int. J. Rem. Sen.*, **16**, 1931-1942.

Rouault, M. and P. A. Durkee (1992). Characterization of aerosols from satellite remote sensing. In *Nucleation and Atmospheric Aerosols*, 357-360, N. Fukuta and P. E. Wagoner (Eds.), A. Deepak Publishing.

Russell, P.B., W. Whiting, P. V. Hobbs and L. L. Stowe (1996). *Tropopsheric Aerosol Radiative Forcing Observational Experiment (TARFOX) Science and Implementation Plan.* NASA Ames Research Center, Moffett Field, CA, 50pp.

Saunders, R. W. and K. T. Kriebel (1988). An improved method for detecting clear sky and cloudy radiances from AVHRR data. *Int. J. Rem. Sen.*, **9,** 123-150.

Schmid, B., J. M. Livingston, P. B. Russell, P. A. Durkee, D. R. Collins, R. C. Flagan, J. H. Seinfeld, S. Gasso, D. A. Hegg, E. Ostrom, K. J. Noone, E. J. Welton, K. Voss, H. R. Gordon, P. Formenti and M. O. Andreae (1999). Clear sky closure studies of lower tropospheric aerosol and water vapor during ACE-2 using airborne sunphotometer, airborne in-situ, space-borne, and ground based measurements. *Tellus,* Submitted.

Shettle E. P., and R. W. Fenn (1979). Models for the aerosols of the lower atmosphere and the effects of humidity variations on their optical properties. AFGL-TR-79-0214 Air Force Geophisics Laboratories, Hanscom AFB, MA.

Swartz, S. E. and M. O. Andreae (1996). Uncertainty in climate change by aerosols. *Science,* **272,** 1121-1122.

Turner, R. (1973). Atmospheric effects in remote sensing. In *Remote Sensing of the Earth Resources, II*, 549-583, F. Shahrocki (ed.), University of Tennessee.

Whiting, W., P. B. Russell, P. V. Hobbs and L. L. Stowe (1996). *Tropospheric Aerosol Radiative Forcing Observational Experiment (TARFOX) Operations Summary.* International Global Atmospheric Chemistry Project (IGAC), 127pp.

INITIAL DISTRIBUTION LIST

No. Copies

1. Defense Technical Information Center.....2
   8725 John J. Kingman Road, Ste 0944
   Ft. Belvoir, Virginia 22060-6218

2. Dudley Knox Library.....2
   Naval Postgraduate School
   411 Dyer Rd.
   Monterey, California 93943-5101

3. Chairman, Code MR.....4
   Department of Meteorology
   Naval Postgraduate School
   Monterey, California 93943-5002

4. Professor Philip A. Durkee (Code MR/DE).....4
   Department of Meteorology
   Naval Postgraduate School
   Monterey, California 93943-5002

5. LT Peter J. Smith.....2
   NAVPACMETOCFAC
   YOKOSUKA, JA
   PSC 473 Box 68
   FPO-AP 96349-2079

6. Mary Jordan 1
   Department of Meteorology
   Naval Postgraduate School
   Monterey, CA 93943-5002